nature sustainability

Article

https://doi.org/10.1038/s41893-024-01306-w

Global peak water limit of future groundwater withdrawals

In the format provided by the authors and unedited

Contents

Global Change Analysis Model

The Global Change Analysis Model (GCAM) is an integrated model used to analyze the evolution of the coupled human-Earth system under global change across multiple environmental, economic, and social dimensions (Calvin et al., 2019). It quantifies information within explicitly represented individual sectors (e.g., water) and their multi-sector interactions across energy, land, climate, and socioeconomic systems. A pillar of the integrated assessment modeling (IAM) approach is to represent individual sectors (e.g., energy, water *etc*.) that permits a greater focus on the interactions between sectors and maintains computational and data tractability. GCAM is a dynamic recursive model that establishes markets for resources, technologies, and physical commodities. For the model to solve in each five-year time step, it seeks to identify prices that equate supply and demand simultaneously across all regional, global, and sectoral markets, including water, electricity, and food. The model's calibration period covers the period from 1975-2015, while 'future' projections occur for the 2020-2100 period (at five-year intervals).

One of the foundational elements of GCAM is its data system, which is comprised of approximately 900 data objects collated from multiple sources (Bond-Lamberty et al., 2019). About 60 of the data objects provide water sector information (e.g., runoff or groundwater supply *etc*.), while 90 data objects from other sectors offer information that indirectly affects water sector dynamics (e.g., water footprint of crops, cooling water demands *etc*.). Just to initialize and calibrate GCAM simulations requires approximately 4000 systematic manipulations of these data objects (Bond-Lamberty et al., 2019). The data objects cover multiple sectors and systems at both global and regional scales, including various agricultural and land use estimates, emissions inventories, energy balances, socioeconomic indicators, and water technologies and supply and demand projections. Historical trajectories are utilized to calibrate GCAM outputs until a base year, after which the recursive dynamic partial-market equilibrium solution of GCAM is activated to project multi-sectoral variables into the future across multiple scales.

GCAM simulations maintain global coverage, but GCAM uses regions (that vary in scale by sector) as its spatial units. For instance, markets are simultaneously solved in 384 agriculture and land use regions, 235 water basins, and 32 energy-economy regions. To solve, the model seeks vectors of prices in each market that equate supply and demand simultaneously across all regional and global markets. Fig. S1 shows major sectors and their sub-systems represented in GCAM in the form of a wireframe diagram. The figure highlights sectoral interactions, along with stylized examples of typical model inputs that drive the model's sectoral interactions and its resulting outputs. Note that Fig. S1 is stylized for illustrative purposes; actual model interactions and number of inputs and outputs are difficult to visualize in a single figure, but have been extensively documented in other resources such as (Calvin et al., 2019) and http://jgcri.github.io/gcam-doc/index.html.

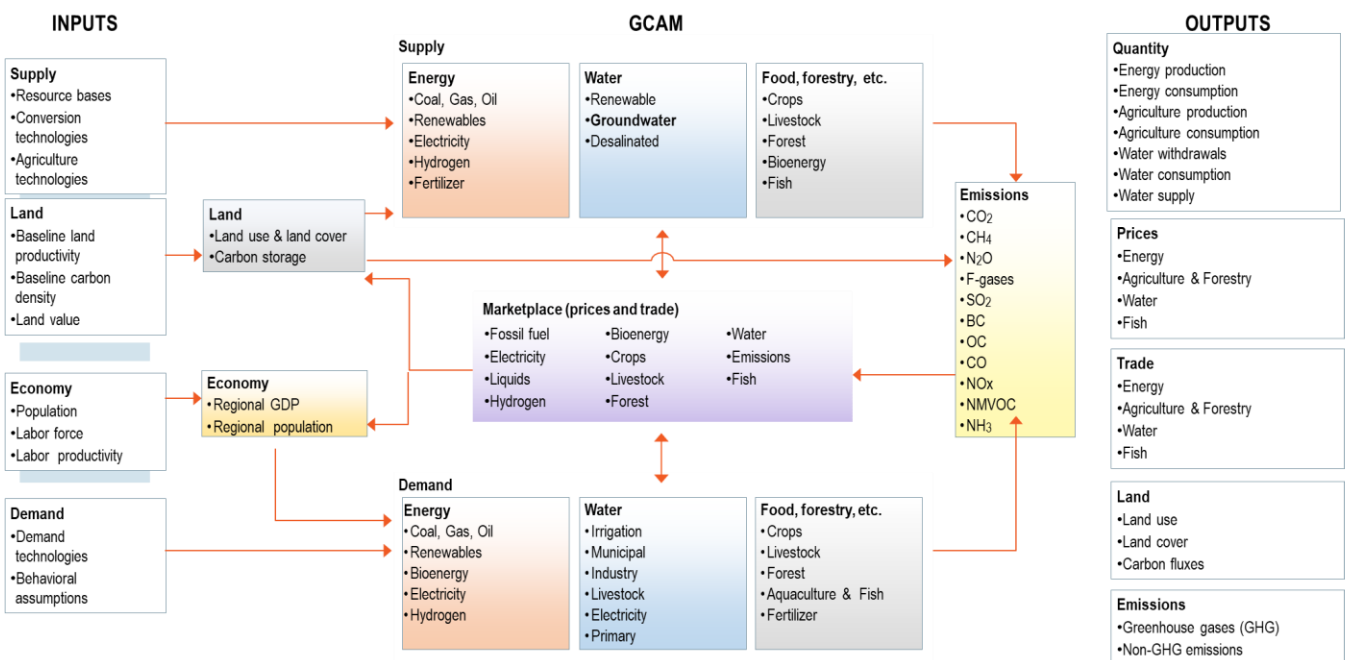

Fig. S1. Overview of the Global Change Analysis Model (GCAM), showing multiple sectors and sub-systems, core sectoral interactions, and examples of key model inputs and outputs (Figure adapted from http://jgcri.github.io/gcam-doc/index.html).

Water Sector in GCAM

The representation of global water supply and demand dynamics in GCAM has been previously described across a large suite of past publications. Here we synthesize that information for readers of the current article, so as to provide a succinct summary of the representation of water dynamics in GCAM.

GCAM operates on a market equilibrium principle, which means the supply of a resource has to equal its demand. Thus, resource equilibrium within GCAM is achieved when demand and supply of a resource equates at a positive price within a spatial region (basins for water markets) during a time period (5-year time period). Water demands (both withdrawals and consumption) across six sectors are driven by bottom-up estimates of productivity in those sectors of the economy—such as agricultural production by crop or withdrawals for cooling by technology. There are three main supply sources that can be used to meet those demands—renewable surface water, nonrenewable groundwater, and desalinated water.

In economics, the term “markets” is used both literally, like the stock market, and figuratively. Water is allocated in both rule-based systems and price-based systems depending on where and when. In rule-based allocation systems, such as in the US west, water is allocated to those with rights. If water cannot be traded, the price that the model generates is the “shadow” price of water. The “shadow price” of water is the economic value that the last unit volume of water has in terms of the water’s contribution to production, for example crops. The shadow price is not published on an exchange somewhere. It is an inferred value of the last unit volume of water’s economic value to its user. The “shadow price” of water may be higher elsewhere, but if the water cannot be traded, the potential gains to trade go unrealized. If we run the water modules within GCAM as a perfectly free market, then the water goes to its highest and best uses.

To reproduce observational water allocations, we use differential water pricing. Water use is subsidized for those with water rights. That shifts water use toward those with water rights. Note that since the water basin is the smallest unit of analysis for GCAM, that water is allocated not to individual holders of the water rights, but to a class of right holders, e.g., farmers in a basin. However, the amount of water in use is determined by the amount physically available. Thus, when a drought occurs in the model, runoff is reduced and the amount of water physically available in the basin is reduced to a new, lower level. The “shadow price” of water rises because farmers cannot use more water than is in the basin, crop production in that basin falls, and the demand for crops and “virtual water” shift to more expensive water sources, such as deeper ground water and to regions that are not experiencing the drought.

This method reflects a couple of key stylized facts. Water is allocated preferentially to certain groups, typically farmers as a class. And, droughts result in unsatisfied demands for water that have consequences—reduced production. This is a major improvement over analyses that simply assign a grid cell the color red when there is unsatisfied water demands but miss both the direct effects of a drought and the indirect, changes resulting from changed agricultural trade patterns and associated virtual water.

Here we provide two examples of a water-related model pathway of interest from Figure S1, highlighting the ways in which socioeconomic, energy, and land system change can propagate back to the water sector through complex multi-system interactions. GCAM has most commonly been used to conduct scenario-based analysis. Consider a scenario in which heterogeneous regional growth in labor productivity (i.e., GDP) and population occurs through 2100. This growth sets the scale of the economy in each of 32 energy-economy regions, driving demands for services. For example, residential buildings will require increasing levels of heating and cooling as population and GDP grow, despite improvements in efficiency of appliances. To provide these services requires an energy carrier, such as electricity, which can compete with other carriers for share of the market meeting end-use energy demands in buildings, industry, and transport. This electricity requires water withdrawal (and potentially consumption) to produce, particularly for thermonuclear technology that has significant cooling needs. This water can be supplied by renewable surface water, groundwater, or desalinated water, each of which has different electricity consumption footprints tracked by the model (Kyle et al., 2021; Liu et al., 2016). As a second example, socioeconomic growth, changing dietary preferences, new strategies for land use and land cover, cultivar improvements, and emissions reduction strategies can increase demands for agricultural production, both to satisfy domestic demands and to meet growing international demands for crops. As these crop patterns shift in the types of crops being grown, and the technology used (e.g., rainfed versus irrigation), the model captures how regional water usage patterns across the three water supply categories shift (at regional resolution, but with global coverage).

Water demand and supply are balanced in each of 235 water basins. Basins are delineated mostly using catchment (i.e., hydrological) boundaries, though in some cases water basins are actually comprised of multiple hydrological basins lumped together. Demands for water are represented across six sectors (Hejazi et al., 2014): irrigation, livestock, electricity production, resource extraction (mining), industry, and domestic (municipal). Basin-level irrigation (i.e., blue water) demands are specified for 12 distinct crop classes (Chaturvedi et al., 2015). Water demands per unit crop produced are gradually reduced over the century to reflect projected water efficiency improvements (Bruinsma, 2009; Turner et al., 2019). In the particular version of GCAM used in this study, all crops are traded freely on a global market. The presence of a water price means that irrigated agriculture may respond to water shortage (and thus an increasing shadow price of water) by shifting to new basins that have a comparative advantage; by more intensively producing crops in areas where irrigation is already deployed; or by shifting from irrigated to rain-fed agriculture, if land is available to do (Turner et al., 2019). Electricity sector water demands can respond to water costs through adoption of efficient cooling technologies or even through shifts away from thermal power plants toward modes of generation that use less water. Domestic water demands—driven primarily by population and GDP—are elastic, forcing users to moderate consumption if prices increase (Hejazi et al., 2013). For all water demand sectors, technology costs, water use coefficients, and consumption efficiencies are specified at regional resolution, compiled from a wide range of data sets, see the full list here: http://jgcri.github.io/gcam-doc/demand_water.html.

Next, we briefly discuss our approach to modeling water supply, with greater emphasis placed on groundwater, given its importance to this particular study.

Water Supply

Water supplies in GCAM come from three sources: renewable water, depletion of nonrenewable (i.e., fossil) groundwater, and desalinated seawater (Turner et al., 2018; Calvin et al., 2019). Aside from desalination, water supply is mainly driven by natural processes, which can include both the active hydrological cycle (e.g., rainfall and runoff) and stocks of non-renewable (i.e., fossil groundwater). Capturing the availability and costs of these resources in each basin, which is an input to GCAM, requires detailed representation of the hydrological cycle and subsurface water availability and extraction dynamics. This is done in external models, such as *Xanthos* for surface and shallow sub-surface hydrology (Liu et al., 2018; Vernon et al., 2019) and *Superwell* for groundwater (Turner et al., 2019).

Renewable Surface Water

Renewable surface water supply accounts for both direct surface water extraction and groundwater pumping that draws on recharged groundwater and captured streamflow. This is the cheapest source of water (on a unit cost basis) available to meet demand in GCAM. In the absence of climate change impacts, the long-term mean annual flow for each basin serves as the upper limit to available renewable supply. This value is computed using mean annual runoff, which is computed at gridded 0.5° spatial resolution in Xanthos. The mean basin flow is taken as an upper limit because it represents the maximum reliable water supply that could be derived from a fully regulated river basin managed to maximize firm yield—meaning water users can readily access the mean flow at all times. Only a portion of the basin flow will be made available for use, depending on environmental flow requirements and installed infrastructure for capturing, transporting, and storing water. This “accessible” portion of renewable water, defined in Eq. S1 below, is calculated for the majority of basins as volume of annual runoff that is potentially stable (meaning available even in dry years; Postel et al., 1996). This volume is determined by simulating the effects of both base flows and in situ storage reservoirs included in the Global Reservoir and Dams inventory (Kim et al., 2016; Lehner et al., 2011), with an allocation of 10% of streamflow for environmental purposes. For instances where estimates of groundwater depletion are available (approximately one fifth of basins), the accessible portion of renewable water is back-calculated from the balance of total water withdrawals and supply from groundwater depletion observed over a historical calibration period.

$$QA_i^t = max\left(0, min\left(QT_i^t - EFR_i, QB_i^t - EFR_i + RS_i\right)\right) \quad \text{Eq. (S1)}$$

where QA_i^t QT_i^t and QB_i^t represent annual volumes of accessible renewable water, natural streamflow and baseflow, respectively, in basin i and year t; EFR_i is the environmental flow requirement for each basin, and RS_i is total reservoir storage capacity in each basin i in the base year (2015 for the version of the model used for this publication). The max in Eq. 1 makes sure the volume does not take negative values, while min allows using the lesser of the net accesible stream flow ($QT_i^t - EFR_i$) and net accesible surface water in any situtation, including droughts ($QB_i^t - EFR_i + RS_i$).

Stream flow and base flow volumes are produced using *Xanthos*, which is a global hydrological emulator operating on the $abcdm$ principle, which captures dynamics between both hydrological fluxes and storages. Parameters a

and b are related to surface runoff characteristics, c and d are related to groundwater characteristics, and m represents snowmelt (Liu et al., 2018; Vernon et al., 2019). *Xanthos* provides all three surface flow timeseries (QA_i^t QT_i^t and QB_i^t) to F.S1, for each of 235 global water basins. This enables calculation of accessible water, and in turn the fraction of total runoff that is accessible, which is provided to end-use sectors at low cost. Using surface water in excess of the renewable fraction becomes increasingly costly, and becomes more comparable on a cost-basis to groundwater extraction.

Nonrenewable Groundwater

Nonrenewable groundwater supply (volume and associated costs of pumping) is generated using a well hydraulics-based groundwater extraction cost model called *Superwell* (Turner et al., 2019). *Superwell* divides the world into 0.5-degree land grid cells, seeking to produce cost curves (i.e., supply curves) that define the cost to cumulatively extract increasing volumetric quantities of nonrenewable groundwater. The model leverages several high-resolution hydrogeologic datasets that have become recently available to estimate the total available volume of groundwater in each grid cell (de Graaf et al., 2015; Fan et al., 2013; Gleeson et al., 2014; Richts et al., 2011). Total aquifer thickness is taken from de Graaf et al. (2015) and depth to water is taken from Fan et al. (2013) to estimate saturated aquifer thickness ($b = aquifer\ thickness - depth\ to\ water$). In particular, aquifer areal extent, thickness, porosity, and head (i.e., water table level) are used to estimate available volumes. The model excludes deeper (>800m) aquifers, since it is fit against measured groundwater head data, though wells deeper than this are unlikely to be economically feasible. As discussed later, we explore several scenarios that constrain depletion to 5%, 25%, and 40% of this total extractible volume, to reflect that there may be evolving socio-environmental preferences to avoid total exhaustion of groundwater resources, as part of a broader transition in freshwater sustainability (Gleick et al., 2018).

After establishing the total physically feasible volume of water that is extractible within a given grid cell, the model then seeks to identify the least cost means of extracting as much groundwater as possible from each grid cell. This is done by successively adding new wells within each grid cell, while accounting for the radius of influence imposed by each well, which is impacted by hydrogeologic factors such as hydraulic conductivity. To identify the relationship between drawdown and extraction rate, the model uses a *Theis* solution and the theory of image wells with superposition. To capture the cost to extract a given quantity of water (while accounting for drawdown and well interference effects), the model calculates a levelized annual cost that accounts for both well installation costs and the costs to lift water from the well to the Earth's surface. This cost relationship is given by Eq. S2 as:

$$C_W = \frac{\left(C_I(1+i)^n \times \frac{i}{(1+i)^n - 1}\right) + 0.07C_I + \left(\frac{\gamma Q^* \left\{ \begin{matrix} iterations\ for\ Q_{max} \\ function\ of\ drawdown \end{matrix} \right\} H}{1{,}000\eta}\right) t_A\ e_r}{Qt} \qquad \text{Eq. (S2)}$$

where C_W is levelized annual unit cost of groundwater extraction, C_I is the initial capital cost of setting up wells that factors in the hydrogeological complexity of the aquifer, i is the rate of interest, n is lifetime of an individual well, Q is optimized groundwater discharge, t is total operational time of well, γ is the specific weight of water, H is the total head (i.e., depth to water plus drawdown), η is the pump efficiency, t_A is the annual operating time of a well, and e_r is the unit cost of energy. *Superwell* combines the modified *Theis* solution with the theory of image wells to capture well dynamics, which then informs cost of extraction under the principle of increasing costs of extraction of deeper groundwater.

As groundwater levels decline due to continuous extraction, the energy required to pump the water to the surface increases, which in turn raises the cost of extraction. Increased pumping makes further groundwater extraction more energy intensive, costing more to pump and effectively becoming an economically less attractive water supply source alternative. This phenomenon is represented in the model using cost curves which relate cumulative volume of pumped groundwater (km3) and unit cost of groundwater ($/km^3). Fig. S2 shows global groundwater extraction costs produced from *Superwell* under three depletion limits as an example. Note similar supply curves are produced for each of 235 global water basins to feed GCAM with nonrenewable groundwater supply information.

Calibration to Historical Groundwater Depletion

The calibration process in GCAM seeks to match the model's groundwater depletion rates with historically observed values of groundwater depletion for basins which exhibit groundwater depletion historically. This procedure is initiated by defining an upper threshold for renewable water in each basin, which is informed by climate datasets, specifically WATCH reanalysis data, and simulated through our hydrological model Xanthos (Liu et al., 2018;

Vernon et al., 2019). The subsequent step involves fine-tuning how much of this renewable water can be accessed for human use, in a way that ensures GCAM's historical depletion aligns with known historical groundwater depletion figures. For basins that show groundwater depletion historically we access accessible fraction using the following equation S3. Refer to Tuner et al. (2019) for in-depth description of groundwater calibration to historical depletion rates.

$$Accessible\ fraction = \frac{water\ demands - groundwater\ depletion}{runoff} \qquad \text{Eq. (S3)}$$

We adjust the accessible fraction of renewable supply, as defined by equation S1, such that the groundwater depletion rate matches historically observed groundwater depletion rates reported by Scanlon et al. (2018) and Gleeson et al. (2012), see equation S3. Because groundwater extraction is calibrated to depletion, by definition it contains embedded groundwater dynamics (e.g., recharge and capture). Importantly, groundwater does not get utilized before the renewable accessible fraction, meaning that the accessible portion of renewable water is cheaper and gets utilized before groundwater use starts. In GCAM simulations, this calibration makes historical withdrawals representative of the said dynamics and provides a realistic initialization to future projections. The calibration process also sets the accessible fraction for the future; assuming fluxes remain largely similar, these dynamics are also represented in future as we keep the accessible fraction constant over time. Note that renewable water supply can change but the accessible fraction remains the same. This means that the portion of these fluxes contributing to the renewal of groundwater are represented in the cheaper source of water supply, which mitigates the concern of over estimation of costs associated with renewed groundwater.

Temporally aggregated cost curves and limits to groundwater depletion

We use a groundwater extraction cost model, as elaborated by equation S2 and published in Turner et al. (2019), to calculate the cost of pumping under hydrogeological controls and varying levels of depletion limits. This simulates drawdown due to produced volume and calculates associated cost of pumping over a 100-year time horizon. As the volume extracted increases, the depth to water (and drawdown) also increases, and thus so does total pumping cost. Within this structure, the rate of aquifer depletion is not entirely relevant for building cost-curves as long as the instantaneous state of depletion is simulated before we temporally aggregate costs into cost bins to convert these to cost curves. This temporal aggregation is done by partitioning costs into discrete bins, summing total volume produced in each cost bin, taking a ratio of both to calculate unit cost (\$/km3), and relating unit cost to cumulative volume produced over all cost bins.

By sampling three alternative levels of depletion limit as part of our experimental design, we capture the uncertainty surrounding varying levels of fluxes resulting in varying levels of groundwater availability. These three cases are collectively representative of a variety of combinations of fluxes (among other factors such a groundwater management practices) that result in various availability levels.

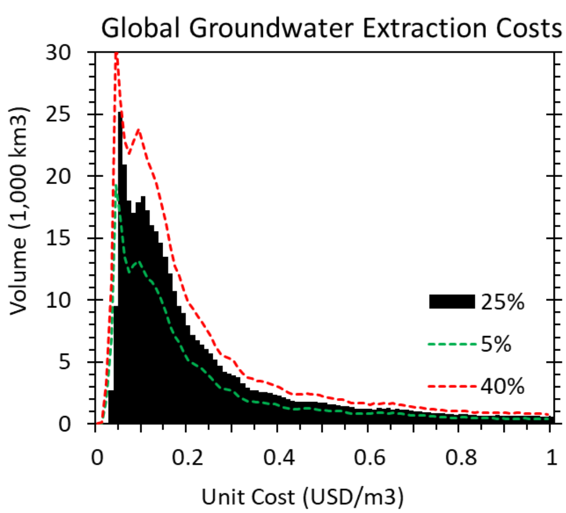

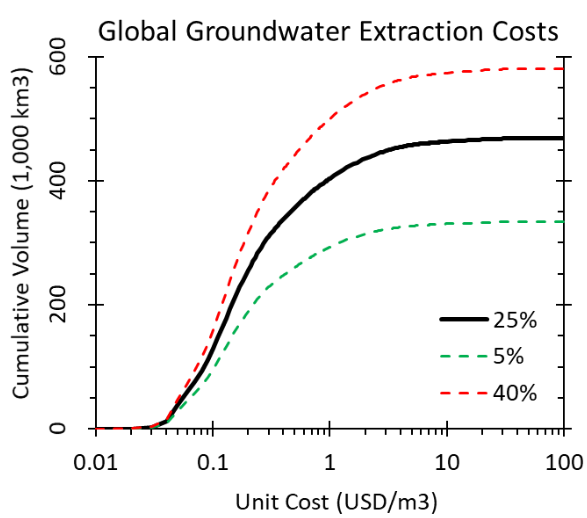

Fig. S2. Global groundwater extraction costs across three groundwater depletion scenarios for an example GCAM water basin: **(a)** extraction volume and unit cost of extraction, and **(b)** cumulative extraction volume and unit cost produced from *Superwell* to provide nonrenewable groundwater supply information to GCAM. 5%, 25%, and 40%

are groundwater depletion scenarios created to limit the maximum groundwater (as a fraction of total groundwater available) allowed to be extracted within a *Superwell* simulation.
Hydrological processes such as groundwater lateral flows, capture, recharge and many other secondary dynamics could alter groundwater accessibility over time. Our study captures these dynamics in an outcome-based modeling framework compared to a process-based modeling framework, see Fig. S3. We capture the outcomes of processes by using scenarios of limits to groundwater depletion, which aim to constrain the pumping volumes to low (5%), moderate (25%), and high (40%) limits of available groundwater. The 5% to 40% range explored in our large ensemble captures a spectrum of potential groundwater availabilities in future that could be manifested through physical processes (e.g., changing fluxes)—such as lateral flows, recharge, capture—or as a consequence of human system dynamics, such as varying groundwater management interventions (e.g., strategies, regulations, etc.).

The pumping dynamics of the limits to groundwater depletion scenarios are modeled in a Theis-based groundwater extraction model to evaluate cost of extraction until the depletion limits are met. (Refer to Turner et al., (2019) for more details). This cost of extraction is then converted to unit cost (total cost divided by total volume produced) and related to cumulative groundwater extracted to create temporally-aggregated groundwater supply-cost curves. Temporal aggregation here suggests that unit costs are divided into cost bins and every unit cost bin contains a volume of groundwater that could be produced within that bin irrespective of the time or rate of extraction. This outcome-based mechanism internalizes the impact of rate of extraction and/or secondary flows such a recharge, capture, and lateral flows, and returns groundwater accessibility-to-cost relations for 235 basins of the world. These groundwater supply-cost curves are fed into our global integrated multisector dynamics model (Calvin et al., 2019) to enable interaction of groundwater with other sectors to account for multi-system (i.e., human-water-food-energy) and multi-scale (e.g., international trade) dynamics that could drive future global groundwater extraction.

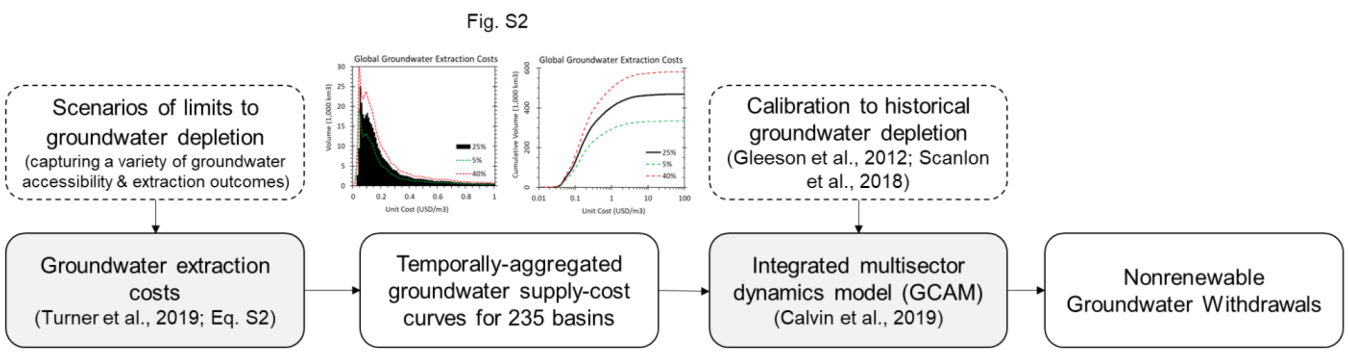

$$C_W = \frac{\left(C_I(1+i)^n \times \frac{i}{(1+i)^n - 1}\right) + 0.07C_I + \left(\frac{\gamma Q^* \left\{ \begin{matrix} iterations\ for\ Q_{max} \\ function\ of\ drawdown \end{matrix} \right\} H}{1{,}000\eta}\right) t_A\, e_r}{Qt}$$

Eq. S2

Fig S3. Physical and economic components for modeling the availability, accessibility, and extraction of nonrenewable groundwater in GCAM.

Desalinated Water
Historical estimates of desalinated seawater supply and associated costs are taken from (Jones et al., 2019) and processed within *gcamdata* to match GCAM spatial resolution of 235 basins and temporal resolutions of 5 year time steps. GCAM incorporates desalinated water as a viable source of freshwater from the purification of brackish groundwater and seawater. The quantification of historical desalinated water production is rooted in data assimilated from FAO Aquastat alongside insights from the study by Jones et al. (2019). The economic aspect of desalinated water requisites electrical energy input along with both the capital and operational expenditures. Given the elevated cost inherent to desalination, this water source becomes a preferred option primarily when the availability of renewable and non-renewable water supplies dwindles, and the expense of freshwater surges. The utilization of desalinated water is made available for municipal and industrial applications mainly due to its high cost. Desalinated water competes with basin water supplies from both renewable and nonrenewable sources on the basis of cost.

Water Demands and Use

Water demands are driven by usage in various sectors and various categories such as municipal, electricity, industrial, and agricultural. GCAM accounts for water usage in six sectors which form water demands in a time period. Four of these sectors, namely, domestic, industry, electricity, and mining, are grouped in non-agricultural water usage, while irrigation and livestock demands are categorized in agricultural water use sectors (Kim et al., 2016). Fig. S4 shows overview of elements of water sector in GCAM, including various water supply sources and water demand categories.

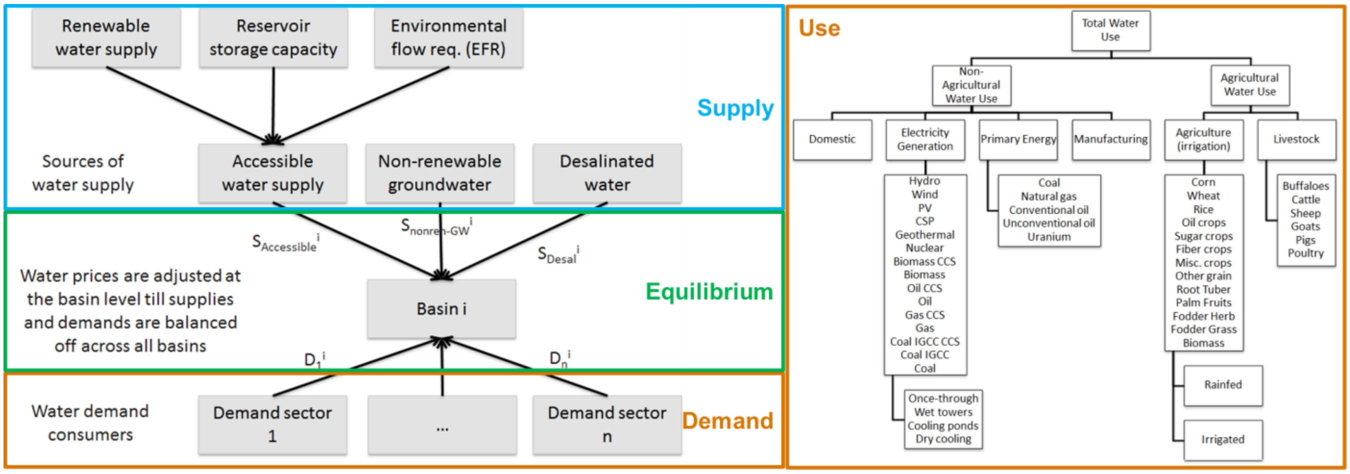

Fig. S4. Overview of water sector within GCAM. Water is supplied in accessible (surface) water, nonrenewable groundwater, and desalinated forms. Water demand is driven by water use in both agricultural and non-agricultural activities. For water markets to solve within GCAM water supply and water demand need to come to an equilibrium within each of the 235 water basins of the world. Adapted from (Kim et al., 2016).

Energy sector demands cover water required by both mining and processing of primary energy and during the generation final energy carriers such as electricity. Both primary energy and electricity generation demands are further broken down by individual energy sources and energy technologies, see Fig. S4 for details. Similarly, irrigation demands are accounted for multiple crop types in both rainfed and irrigated crop categories. Livestock water demands are also accounted for multiple animals, see Fig. S4 for details. This bottom-up accounting of water demands through human water use allows the model to capture connections between the water sector and other sectors such as energy, land, socioeconomics, and climate. Total water demands accumulated in a basin across both agricultural and non-agricultural uses is meant to be met by total water supplies from all three sources to reach an equilibrium.

Scenario design and GCAM sensitivity to RCPs and SSPs

GCAM and RCPs

Representative Concentration Pathways (RCPs) are a set of standard climate scenarios developed to describe the radiative forcing (a measure of the warming effect of greenhouse gases in the atmosphere) that is expected to result from different levels of greenhouse gas emissions. The RCPs are used in conjunction with climate models, including GCAM, to project the future evolution of the Earth's climate under different emission scenarios.

GCAM is often used in conjunction with RCPs to analyze the impacts of different emission scenarios on a range of indicators, including economic, environmental, and social outcomes. The results of these analyses can be used to inform policy decisions and to guide the development of strategies for mitigating and adapting to the impacts of climate change. We have used standard RCP4.5 as it was originally developed using GCAM, and have implemented RCP2.6, RCP6.0, and RCP8.5 in GCAM using the method mentioned in Table S1.

Table S1. Implementation philosophy and interpretation of RCPs in GCAM. Every model version might have slightly different trajectories. Data and table from (Thomson et al., 2011).

RCP2.6	RCP4.5	RCP6.0	RCP8.5
Climate scenario with total radiative forcing in 2100 of 2.6 W/m^2. This value is exceeded prior to 2100	Climate scenario that stabilizes total radiative forcing at 4.5 W/m^2 by 2100	Climate scenario that stabilizes total radiative forcing at 6.0 W/m^2 after 2100	No climate scenario where total radiative forcing reaches 8.5 W/m^2 in 2100. This is achieved by holding technology cost & performance constant and equal to 2005 values

RCPs affect multiple elements in energy, land, atmosphere, and climatic domains spanning from different energy production and consumptions trends for each technology, greenhouse gas (GHG) emissions, atmospheric concentrations of GHGs, radiative forcings, land use and land cover types, and prices of carbon and energy sources. About 90 different trajectories are quantified in GCAM which show sensitivity to different RCPs, but a handful are shown in Fig. S5 for illustrative purposes.

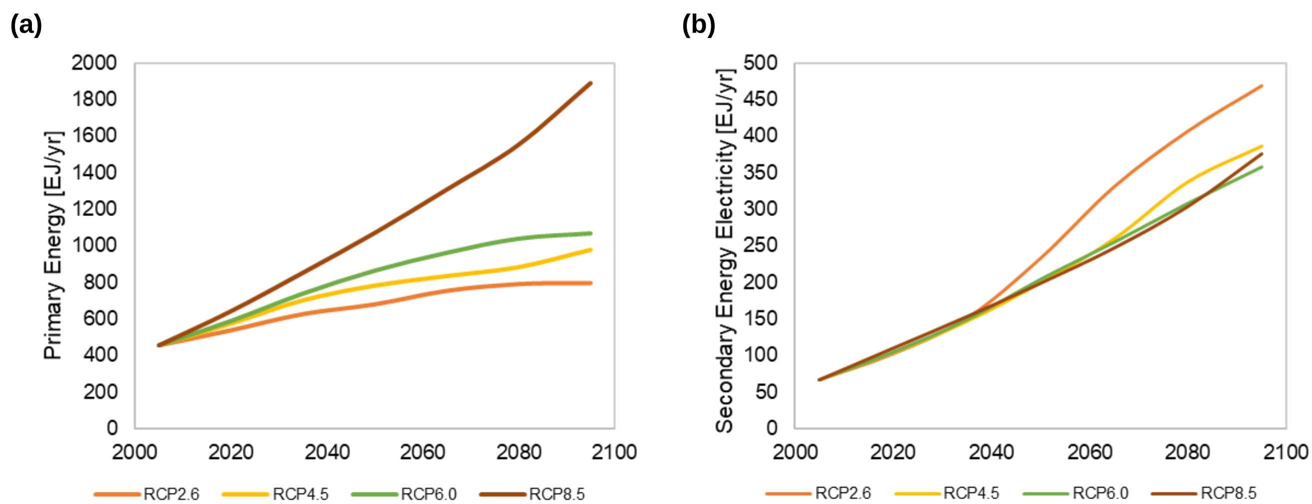

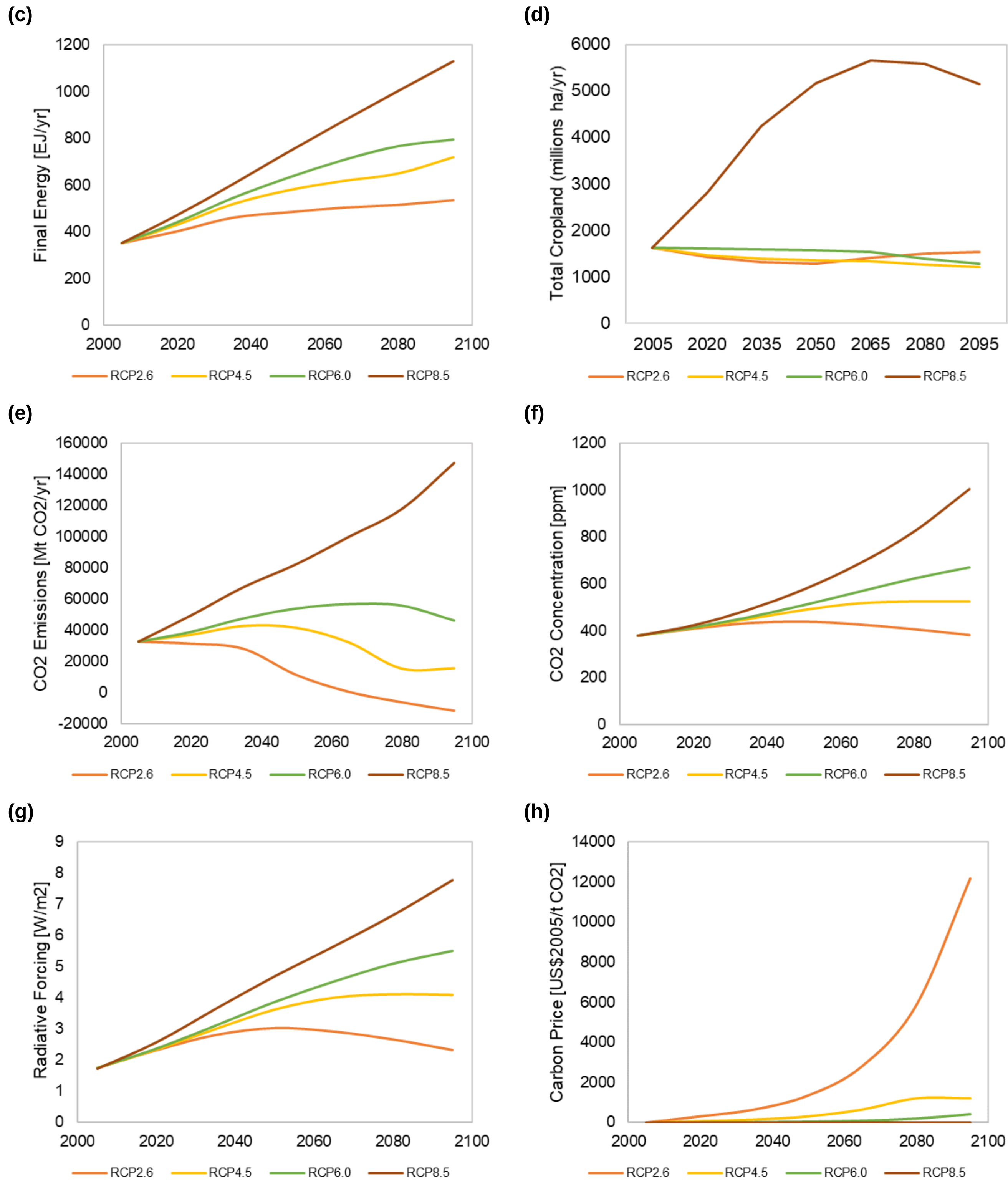

Fig. S5. Some key trends in GCAM under various RCPs reported by (Thomson et al., 2011). **(a)** Primary energy, **(b)** Secondary energy electricity, **(c)** Final energy, **(d)** Total land cover under cropland, **(e)** CO2 Emissions, **(f)** CO2 Concentration, **(g)** Forcing, and **(h)** Carbon price.

GCAM and SSPs

Shared Socioeconomic Pathways (SSPs) are a set of standard socioeconomic scenarios developed to describe different pathways for future socioeconomic and demographic development and the drivers (such as population and GDP) that will shape these pathways. The SSPs are based on a range of assumptions about factors such as population growth, economic development, technological change, and resource availability, and they are used in conjunction with climate and integrated assessment models, including GCAM, to project the future evolution of the Earth's climate and resources under different development scenarios. The five standard SSPs are:

- SSP1: Sustainable development with low population growth, green technologies, and global cooperation.
- SSP2: Middle-of-the-road development with gradual income growth and technological progress, and balanced use of resources.
- SSP3: Regional rivalry and inequality with high population growth, low economic development, and fragmented governance.
- SSP4: Inequality and fossil-fueled development with high inequality, slow technological progress, and heavy reliance on fossil fuels.
- SSP5: Fossil-fueled development and high emissions with high economic growth, rapid technological progress, and heavy reliance on fossil fuels.

GCAM is often used in conjunction with SSPs to analyze the impacts of different development scenarios on a range of indicators, including economic, environmental, and social outcomes. The results of these analyses can be used to inform policy decisions and to guide the development of strategies for mitigating and adapting to the impacts of climate change. Fig. S6 shows some trends of drivers and underlying assumptions consistent with baseline SSP narratives taken from SSP Database v2.0 https://tntcat.iiasa.ac.at/SspDb/dsd?Action=htmlpage&page=20.

(a)

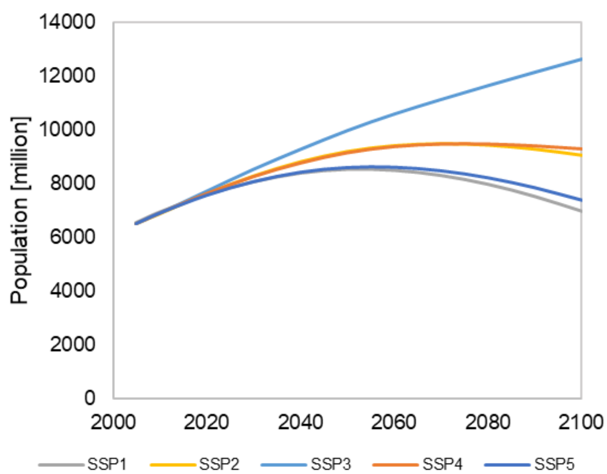

(b)

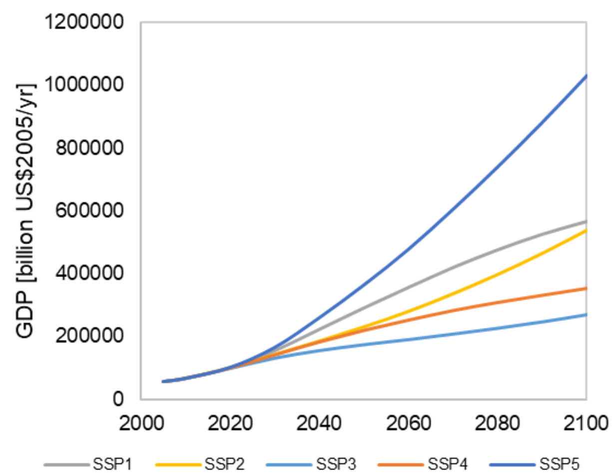

(c)

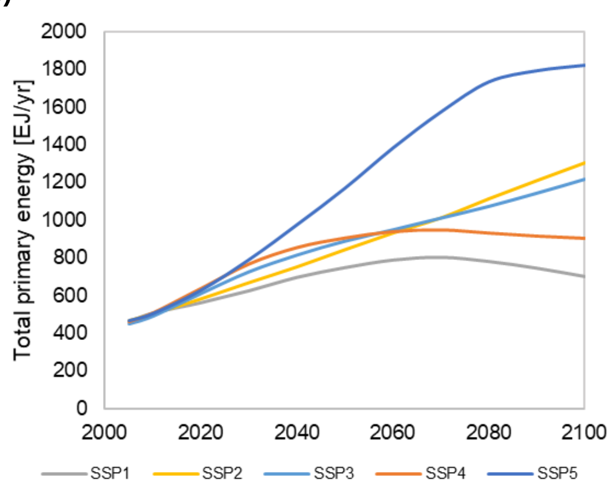

(d)

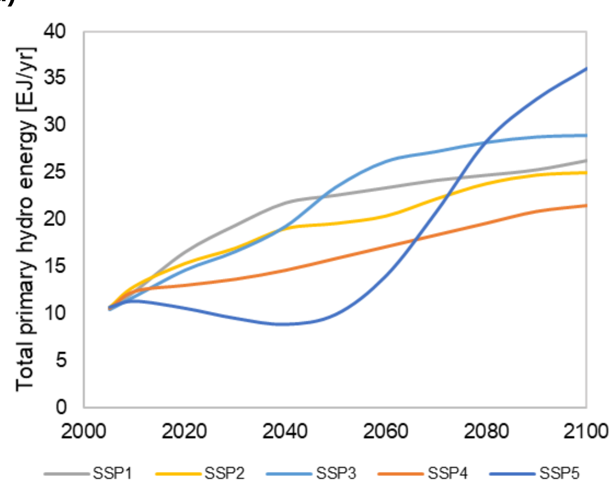

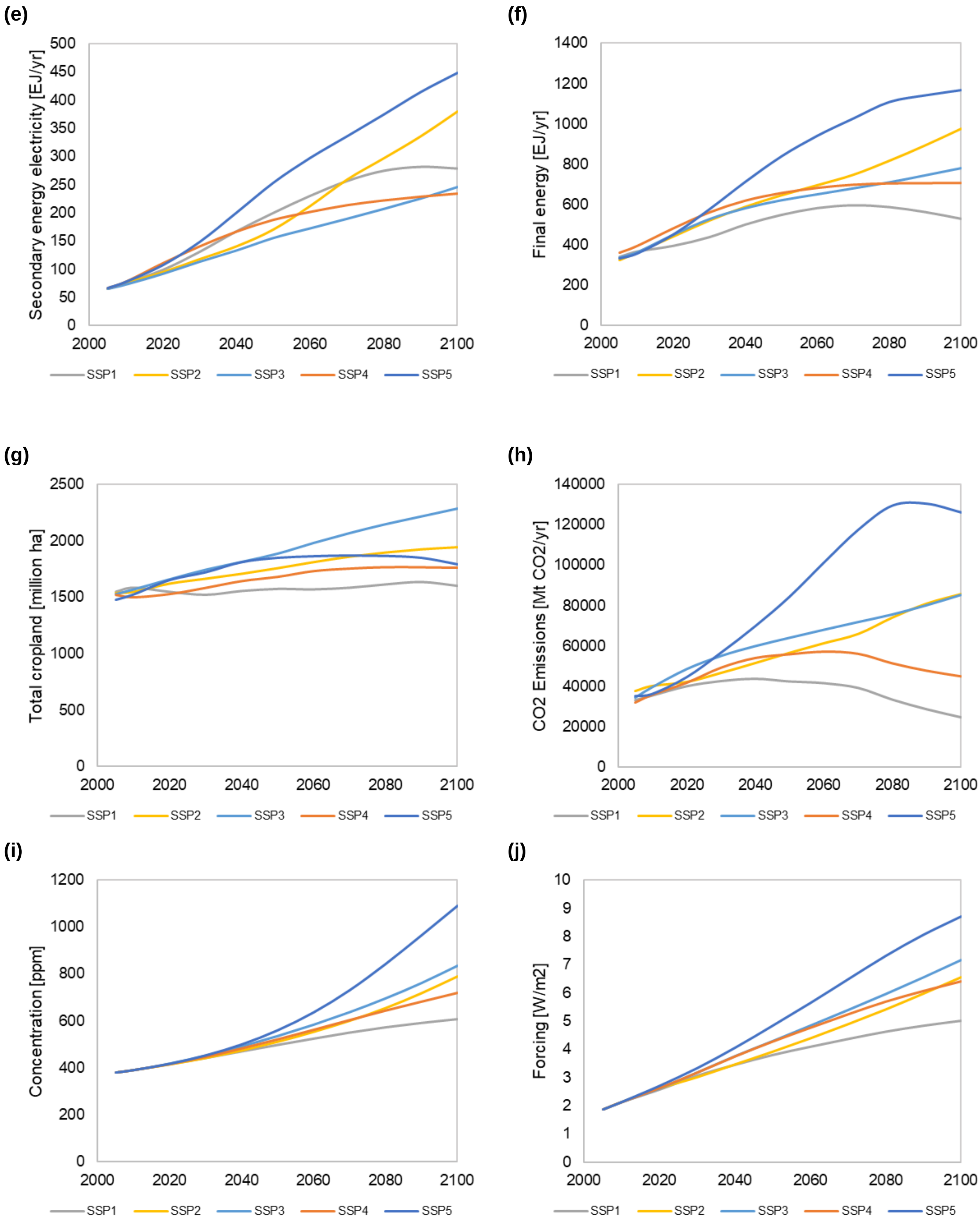
(e)
Secondary energy electricity [EJ/yr]
SSP1 SSP2 SSP3 SSP4 SSP5
(f)
Final energy [EJ/yr]
SSP1 SSP2 SSP3 SSP4 SSP5
(g)
Total cropland [million ha]
SSP1 SSP2 SSP3 SSP4 SSP5
(h)
CO2 Emissions [Mt CO2/yr]
SSP1 SSP2 SSP3 SSP4 SSP5
(i)
Concentration [ppm]
SSP1 SSP2 SSP3 SSP4 SSP5
(j)
Forcing [W/m2]
SSP1 SSP2 SSP3 SSP4 SSP5

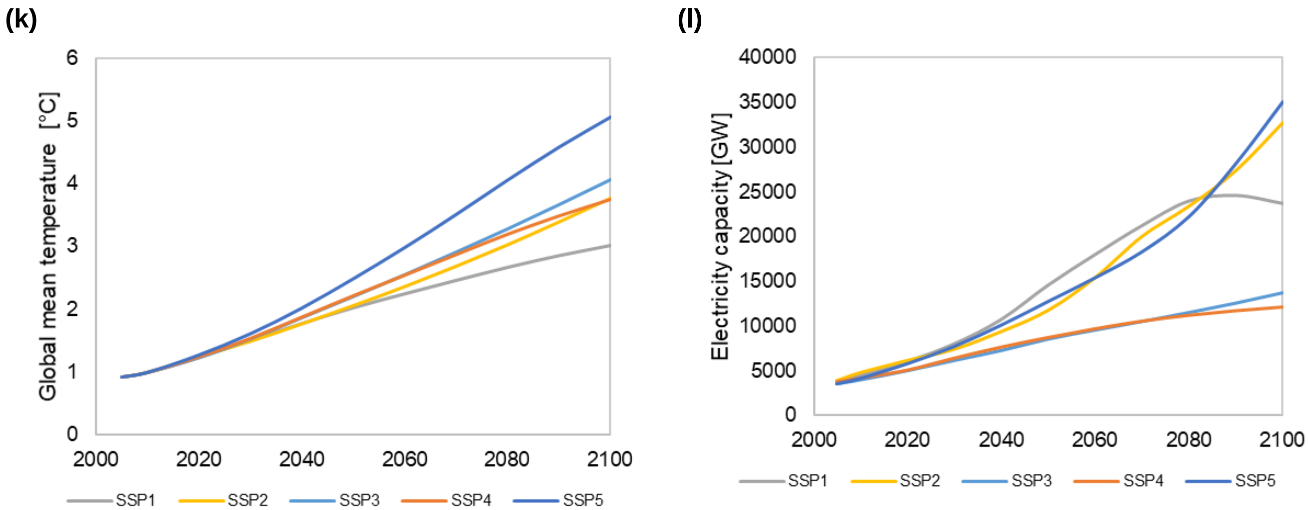

Fig. S6. Some drivers and underlying assumptions of baseline shared socioeconomic pathways globally: **(a)** Population, **(b)** Gross domestic product (GDP), **(c)** Total primary energy, **(d)** Total primary energy in the form of hydropower, **(e)** Secondary energy in the form of electricity, **(f)** Total final energy for end-use, **(g)** Total land cover in the form of cropland, **(h)** Carbon dioxide emissions, **(i)** CO_2 concentration, **(j)** radiative forcing, **(k)** global mean temperature, and **(l)** total electricity capacity.

Consistent assumptions inherent to SSPs, such as the relative ease of technological adoption or phasing out of fossil fuels, along with other assumptions as shown in Table S2, impact the sectoral evolution within GCAM, however population and GDP assumptions especially impact the demands within GCAM. In our model, demands are a function of both population (P) and GDP, as shown in the equation below. This could be the driver behind varying peak-and-decline dynamics across basins. For instance, SSP1 has the lowest population among all SSPs but has higher GDP than others, except SSP5, indicating that fewer people, but with higher incomes, are driving the demands. These coupled drivers drive the demand of groundwater, and, due to lower population and higher incomes in SSP1, it results in earlier peaks. Additionally, each of the other SSP scenarios continue to have population growth through at least 2070, which further increases the demand for water resources across end-use sectors in those SSPs. Other water related policies and management practices, such as the degree of water use efficiency and water-saving technological adoption, could lead to earlier implementation of water-saving measures or alternative water supply sources, such as desalination or water reuse, hence reducing the dependency on nonrenewable groundwater resources much earlier.

$$D_{i,t} = D_{i,2015} \bullet \left(\frac{GDP_t}{GDP_{2015}}\right)^{income-elasticity} \bullet \left(\frac{P_t}{P_{2015}}\right)^{price-elasticity} \qquad \text{Eq. (S4)}$$

SSP-relevant water sector assumptions were also incorporated in GCAM to make water demand patterns more consistent with the overall SSP storylines (Graham et al., 2018). Specifically, water use efficiency for irrigation, energy, and manufacturing sectors, along with technological change in water sector were implemented. Table S2 shows overall SSP storylines along with water sector medication implemented in GCAM (Graham et al., 2018; O'Neill et al., 2014; Riahi et al., 2017). Refer to (Graham et al., 2018) for detailed explanation and quantitative changes associated with qualitative assumptions shown in Table S2.

Table. S2. Some key trends in GCAM under various SSPs. Adapted from (Graham et al., 2018)

Qualitative Assumptions for the SSP Scenarios Within GCAM (All Nonwater Sector Assumptions Adopted From Calvin et al., 2017)

		SSP1	SSP2	SSP3	SSP4 High income	SSP4 Medium income	SSP4 Low income	SSP5
SSP prescribed challenges	Challenges to mitigation	Low	Medium	High	Low			High
	Challenges to adaptation	Low	Medium	High	High			Low
Socioeconomics	Population in 2100	6.9 billion	9 billion	12.7 billion	0.9 billion	2.0 billion	6.4 billion	7.4 billion
	GDP per capita in 2100	$46,306	$33,307	$12092	$123,244	$30,937	$7,388	$83,496
Fossil resources (technological change/acceptance)	Coal	Med/Low	Med/Med	High/High	Med/Low	Med/Med	Med/High	High/High
	Conventional gas and oil	Med/Med	Med/Med	Med/Med	High/Low	High/Low	High/Low	High/High
	Unconventional oil	Low/Med	Med/Med	Med/Med	Med/Low	Med/Low	Med/Low	High/High
Electricity (technology cost)	Nuclear	High	Med	High	Low	Low	Low	Med
	Renewables	Low	Med	High	Low	Low	Low	Med
	CCS	High	Med	Med	Low	Low	Low	Low
Fuel preference	Renewables	High	Med	Med	High	High	High	Med
	Traditional biomass	Low	Low	High	Low	Low	High	Low
Energy demand (service demands)	Buildings	Low	Med	Low	High	Med	Low	High
	Transportation	Low	Med	Low	High	Med	Low	High
	Industry	Low	Med	Low	High	Med	Low	High
Agriculture and land use	Food demand	High	Med	Low	High	Med	Low	High
	Meat demand	Low	Med	High	Med	Med	Med	High
	Productivity growth	High	Med	Low	High	Med	Low	High
	Trade	Global	Global	Global	Regional	Regional	Local	Global
Water use (efficiency improvements)	Irrigation	High	Med	Low	High	High	Low	High
	Manufacturing	High	Med	Low	High	Med	Low	High
	Energy	High	Med	Low	Med	Med	Med	High
Water (technological change)	Shift to recirculating and dry cooling	High	Med	Low	High	Med	Low	High
	Municipal	High	Med	Low	High	Med	Low	High
	Municipal water price	Med.	Med	High	Low	Med	High	Low

Design of Experiment

Study's Objectives and the Experimental Design

The overarching goal of this paper is to test our hypothesis that nonrenewable groundwater may exhibit peak-and-decline behavior in line with what has been historically observed for other depletable resources (e.g., minerals). To our knowledge this is the first attempt to quantify the potential for this behavior, and doing so is an important step towards recognizing the challenges surrounding human-groundwater interactions and sustainability. We intended to better understand where and when peak in groundwater withdrawals could emerge by using a wide array of uncertain human and Earth system forces that might play a role in influencing the emergence of peak-and-decline. So, we designed and executed what is, to our knowledge, the most computationally intensive groundwater-focused large ensemble experiment ever conducted in the context of a coupled human-Earth system model (in our case, we used GCAM). Our design of experiment included a full combinatorial sampling of the entire suite of uncertain human and earth system (i.e., demand and supply) drivers we considered (see Figure 4 in main text). In other words, each uncertain factor was permutated with every other factor, to generate a large ensemble of scenarios describing a wide range of plausible global groundwater futures. We excluded infeasible ensemble combinations from our full combinatorial scenario matrix. For example, it is not possible to achieve RCP8.5 climate forcing under SSP1 through SSP4 socioeconomic and technological assumptions, so we excluded these scenarios. Likewise, it is not possible to mitigate to a RCP2.6 forcing level under SSP3 assumptions. As a result, each scenario maintained internal consistency with all its constituent ensemble members (e.g., SSPs and RCPs) while also remaining independent from other possible futures generated by other ensemble members.

Exploratory Modeling

Our study applies exploratory modeling, which is growing in the global change literature (Guivarch et al., 2016; McJeon et al., 2011; Rozenberg et al., 2014; Weaver et al., 2013; (Lamontagne et al., 2018) and GCAM-focused (e.g., (Birnbaum et al., 2022; Dolan et al., 2021; Lamontagne et al., 2018); Giuliani et al., 2022; Woodard et al., 2023; Huang et al., 2023). This is because it is well-suited for analyzing deep uncertainties (Knight, 1921; Walker et al., 2003), or those to which it is difficult or impossible to credibly assign probabilities (or probability distributions). Deep uncertainties concerning the internal state and dynamics of the human–Earth system make a priori hypothesis falsification and assessments of scenario likelihood extremely difficult (Lamontagne et al., 2018). Many of the uncertain factors central to the future of groundwater extraction (e.g., climate change) that we sample in our experiment are forms of deep uncertainty. Thus, exploratory modeling prevents our imperfect perceptions of what is probable from limiting our exploration of what is possible. Ultimately, our large ensemble is useful for evaluating the robustness of our conclusions regarding whether, when and where peak-and-decline behavior is exhibited, rather than for evaluating its likelihood.

We purposefully do not assign levels of likelihood to uncertain factor inputs, and thus does not assign probabilities to each scenario (or its outcomes) in the large scenario ensemble. That is, we generate diverse but plausible scenarios without assigning probabilities. Assigning likelihood to plausible futures sits at the frontier of scenario science and exploratory analysis research, and thus remains too under-developed a science for its application here. There have been some attempts in the past to estimate the likelihood of forces such as climate futures (Huard et al. 2022; Ho et al. 2019), but most of these studies have either relied on expert judgement or acknowledge severe methodological limitations and/or extreme contrasts in results. Regardless, implementing such an approach is generally understood to be in contradiction with the idea of scenario-based exploratory analysis (Moss et al., 2010; O'Neill et al., 2014; Riahi et al., 2017).

Scenario Design

Exploration of future resource evolution requires capturing multisector interactions under multiple futures. Such pathways of possible futures are referred to as scenarios. 900 GCAM scenarios were designed to explore evolution of groundwater withdrawals over the 21st century. Scenarios design framework for 900 GCAM simulations is shown in Fig. S7. These 900 scenarios were designed using a full factorial sampling of five Shared Socioeconomic Pathways (SSPs), four Representative Concentration Pathways (RCPs) of climate forcing, five global climate models (GCMs), three groundwater depletion limits, two surface water storage expansion regimes, and two trends of historical groundwater deletion which were also used for model calibration. Some SSP-RCP scenarios do not coexist together as these SSPs do not cause the end of the century climate forcing to reach those particular RCP levels. Such combinations are denoted as not feasible in Fig. S7 (b).

(a)

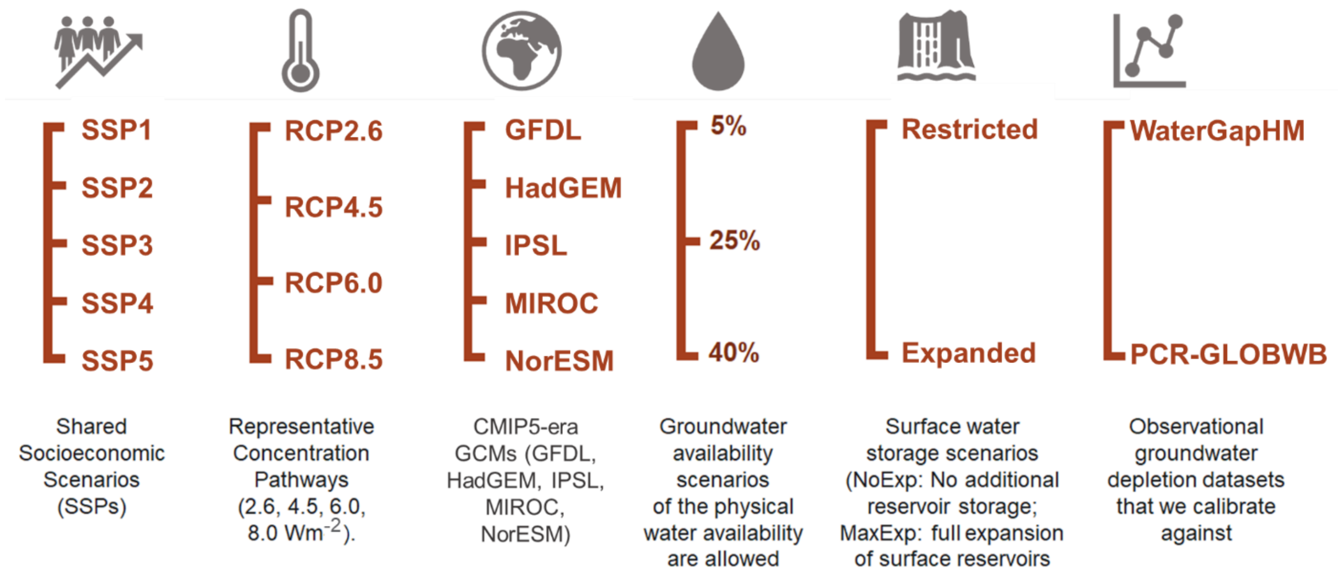

Peak year in feasible SSP & RCP combinations		**Socioeconomic Scenarios** (Shared Socioeconomic Pathways)				
		SSP1	SSP2	SSP3	SSP4	SSP5
Climate Scenarios (Representative Concentration Pathways)	RCP 8.5	Not feasible	Not feasible	Not feasible	Not feasible	2050
	RCP 6.0	2045	2070	2100	2055	2065
	RCP 4.5	2050	2070	2100	2065	2060
	RCP 2.6	2060	2060	Not feasible	2080	2055

Fig. S7. (a) Scenarios design for the large ensemble GCAM simulations, **(b)** feasible combinations of shared socioeconomic pathways (SSPs) and representative concentration pathways (RCPs) along with their maximum peak year values.

Interpretation of Scenarios

Our scenarios are intended to represent a diverse range of plausible futures, but are not predictions, and by extension the outcomes of our scenarios are also not predictions. Instead, the outcomes are "what-if" evaluations under plausible futures represented through scenarios.

Water Specific Scenario Assumptions

Apart from SSPs and RCPs, the scenario design included four dimensions of uncertain water futures. These water-specific scenario dimensions include impacts of alternative climate pathways on water systems, historical groundwater depletion trends used for model calibration, scenarios for future groundwater depletion limits, and surface water storage expansion regimes.

Historical Groundwater Depletion Rates

Trends of resource production or consumption reported or measured historically are utilized in GCAM to calibrate its resource availability and evolution before a base year. These datasets are used to tune the model, so it captures correct historical dynamics which form the basis of future projections in a model simulation. Groundwater withdrawals are calibrated using previously reported datasets of groundwater depletion rates (Gleeson et al., 2012; Scanlon et al., 2018). These datasets are utilized to calculate historical depletion for each of the 235 water basins. This depletion trend is then used to adjust the accessible fraction of surface water, which then determines the portion of surface water supply that is relatively cheaper than the rest of the surface water. Surface water would then compete with nonrenewable groundwater supply in the marketplace for future timesteps. Thus, the threshold price at which groundwater becomes relatively cheaper source of freshwater is sensitive to the data used for calibration of historical groundwater withdrawals. This sensitivity bridges the historical availability and human use of groundwater to the future groundwater withdrawal trajectory.

Groundwater Depletion Limits

Future groundwater availability scenarios were made by constraining the maximum amount of groundwater volume that could be extracted over the 21st century. 5%, 25%, and 40% fractions were used to in the three groundwater depletion scenarios. These scenarios build on the groundwater depletion scenarios explored in (Turner et al., 2019). Through Function S2 the constrained maximum groundwater withdrawal volume translates into cost of extraction, which is then used as an input to GCAM. See Fig. S2 for cost curves of groundwater supply under various future depletion scenarios.

Climate Impacts on Water Resources

Climate change effects water resources on multiple fronts including the hydrological cycle elements such as precipitation, evapotranspiration, soil moisture, snow melt *etc*. For the scope of this study, these elements interact and culminate to surface water runoff, which is later fed into GCAM as an input. A method chain was developed to ‘propagate’ climate impacts to surface water runoff which was eventually used by GCAM to study groundwater evolution. The process of taking climate impacts data from Inter-Sectoral Impact Model Intercomparison Project (ISIMIP), passing it through Xanthos to get surface water runoff to be eventually used by GCAM as an input is presented hereunder:

- Convert data from raw ISIMIP climate data to Xanthos required format. Required climate variables for Xanthos are precipitation, air temperature, minimum air temperature, relative humidity, longwave and shortwave radiation, and wind speed.
- Obtain "observed" historical runoff from VIC (or other Global Hydrologic Model like WaterGap2) forced by the same climate forcing. Check and process this data to Xanthos required format.
- Calibrate Xanthos using historical climate data and runoff observation
- Validate the calibrated output, make sure Xanthos performance is acceptable
- Run Xanthos with future climate forcing (CMIP6 GCMs/RCPs) to get future projections of runoff
- Post-process Xanthos runoff (e.g., smoothing the output) for GCAM's purpose.
- Run GCAM

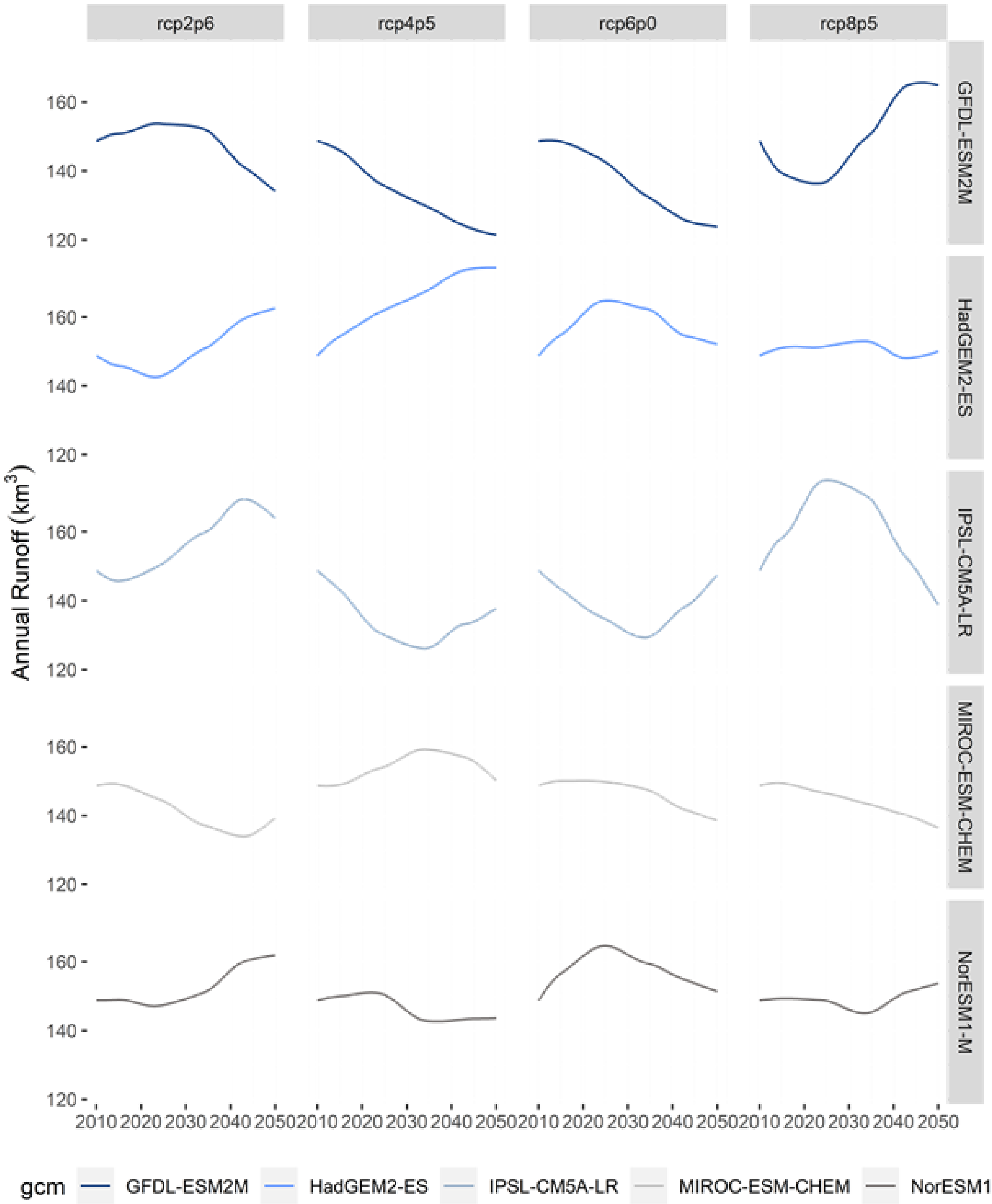

Fig. S8. Different combinations of future climates (RCPs on top) and climate impacts (5 models on right) on annual surface water runoff for Indus basin. Similar runoff combinations were provided as an input for all 235 basins.

Surface Water Storage Expansion Regimes

Surface water reservoirs provide greater degree of control over water supply during anomalous conditions. Two scenarios for surface water storage expansion were considered, including a restricted scenario in which historical surface water storage is maintained throughout the century, and an expansion scenario in which surface water storage reserves are allowed to expand to its full capacity over the 21st century. Constrained cost curves, as shown in Fig. S9(a), are used which represent the cost of water usage as per each fraction of available water. Available fraction is the ratio between accessible water and total runoff, see F.S1 for explanation of terms. The runoff trajectories shown in Fig. S9(b) for each of the expanded and restricted scenarios are used in conjunction with the available fraction to calculate overall cost of water withdrawals.

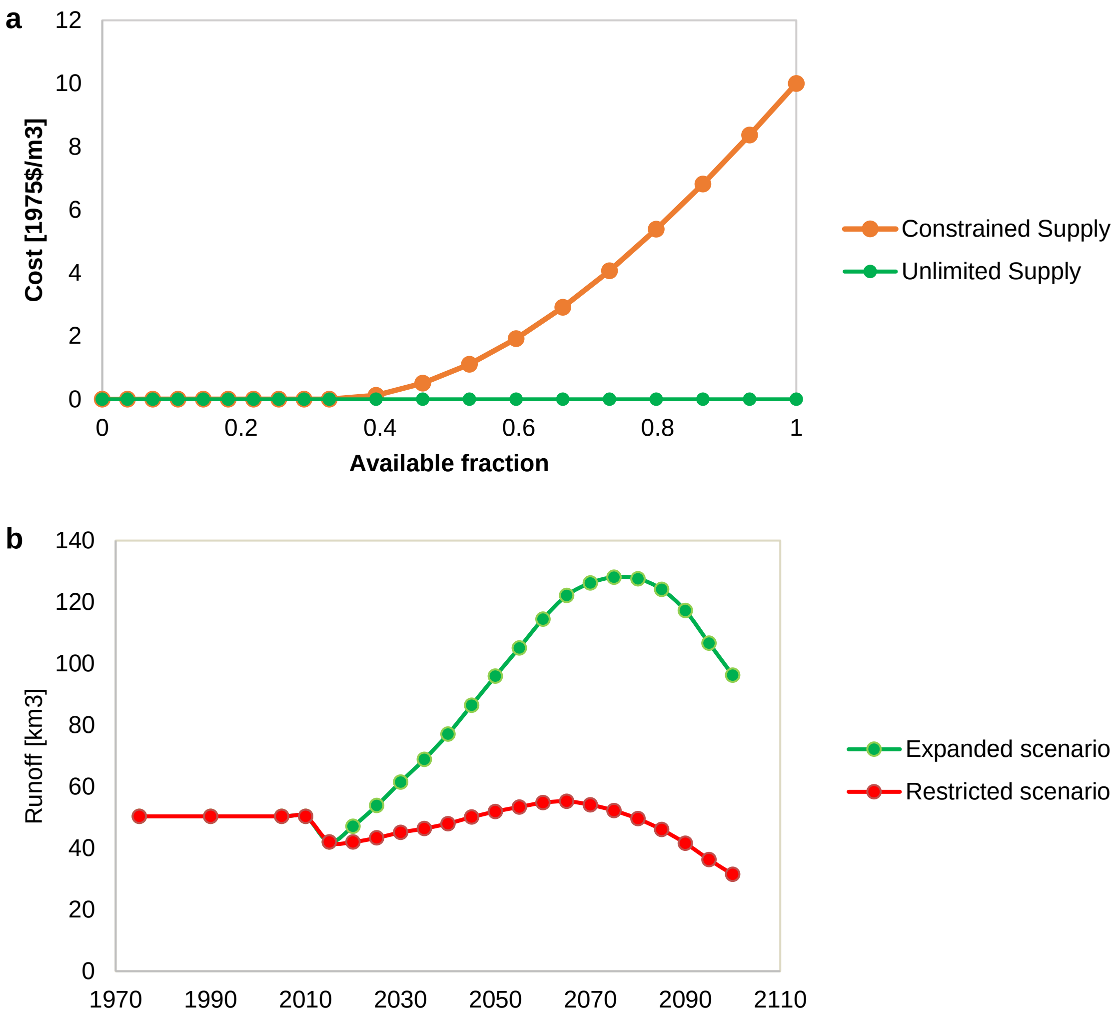

Fig. S9. Implementation of expanded and restricted scenarios using cost curves and maximum runoff for Arabian Peninsula: **(a)** surface water runoff supply and cost curves for unlimited supply and constrained supply cases, and **(b)** annual maximum runoff in Arabian Peninsula basin in eastern Africa for surface water storage expansion (green) and restricted scenarios (red). Similar runoff trends were used as an input for all 235 basins.

Analysis Approach

Our analysis focuses on fossil groundwater because it is effectively a non-renewable resource, having accumulated over many thousands of years, with very limited prospect of being replenished during human-relevant time frames. Renewable flows of water in the rivers, lakes, and wetlands that constitute the active hydrologic cycle are flux-limited (Abbott et al., 2019; Oki & Kanae, 2006), and are thus less likely to exhibit this behavior.

The rigorous modeling exercise produced extensive results (≈ 4.36 million data points) which, like other large ensemble exploratory modeling and scenario discovery exercises, could have been analyzed in many ways. Our analysis spans three dimensions: space, time, and scenarios. In the space dimension we present global peak and decline by aggregating across all basins and all scenarios (Fig. 1 in main text) to analyze if peak and decline is happening globally in all possible futures. In the time dimension all model results span from 2010 till 2100, but later in Fig. 3 of main text, we focus on extremes and present peak year in each scenario categorized by SSPs and RCPs. In the scenarios dimension we show (a) percentage of scenarios in which each basin is showing peak and decline (Fig. 2 in main text) to analyze where peak-and-decline behavior is occurring, and to identify if this is a spatially isolated pattern, and (b) variation of peak year and peak water in each scenario to see how peak year and peak water vary across key dimensions of human and Earth system uncertainty (Fig. 3 in main text).

Validation using Historical Groundwater Depletion Estimates

Groundwater withdrawals produced from 900 GCAM runs were validated against previously reported historical groundwater depletion estimates. Table S3 shows the studies and depletion rates reported for different years. Fig. 1 in main text shows the groundwater withdrawal estimates produced from GCAM runs agree well with historically reported groundwater depletion rates. Future estimates of groundwater depletion from these studies do not reveal a consistent trend when compared among studies, however most of these estimates fall within the 90% band of empirical distribution across estimates from 900 GCAM scenarios.

Table S3. Historical groundwater depletion rates from literature used for validation of GCAM simulations.

Study	Depletion [km^3/yr]	Year
(Wada et al., 2010)	126	1960
	283	2000
(Konikow, 2011)	145	2004
(Wada et al., 2012)	64	1960
	204	2000
	295	2050
(Pokhrel et al., 2012)	455	2000
(Döll et al., 2014)	113	2004.5
(van Dijk et al., 2014)	92	2007.5
(Wada & Bierkens, 2014)	90	1960
	304	2010
	597	2099
(Yoshikawa et al., 2014)	216	1960
	510	2000
	1115	2050
(Pokhrel et al., 2015)	330	2000
(de Graaf et al., 2017)	137	1985
(Dalin et al., 2017)	292	2010
(Hanasaki et al., 2018)	182	2000

Groundwater Peak-and-Decline across 900 GCAM scenarios

This paper presents the peak-and-decline pattern of nonrenewable water extraction over the 21st century. Fig. 1 in the main text provides empirical quantiles of the global nonrenewable water withdrawals across all 900 scenarios encompassing human-earth dimensions modelled using Global Change Analysis Model (GCAM). Here, in Fig. S10 original trajectories of the 900 scenario results are shown for illustrative purpose based on which the empirical quantiles of Fig. 1 are calculated. Two distinct starting points in 2010 appear because the model calibration of historical outputs was done using two different model datasets to achieve better accuracy in future projections.

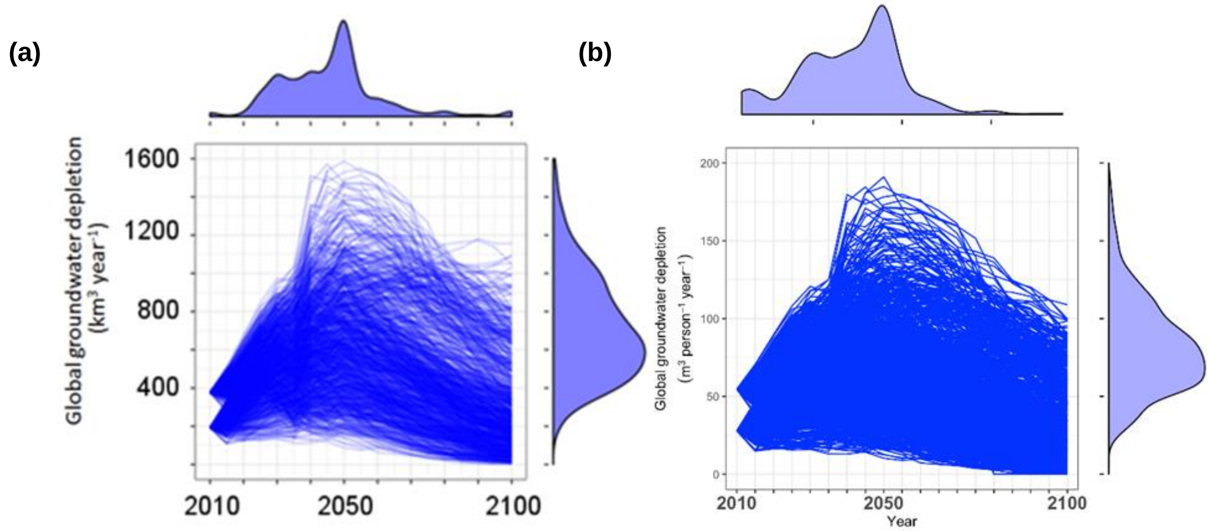

Fig. S10. Individual trajectories for 900 GCAM simulations (a) annual global groundwater depletion rate (km3 year-1), and (b) annual per-capita global groundwater depletion rate (m3 person-1 year-1), with the distributions of the time to peak (pdf on top), and the peak annual groundwater depletion rate (pdf on right) during the 21st century. The historical discontinuity around 2010 occurs due to two alternative historical global groundwater withdrawal datasets used for calibration.

Example trajectories of two of the 21 ensemble members (across 6 categories) of the experiment design are shown in Fig. S11. The variation of these ensemble members individually, while keeping all other ensemble members unchanged, facilitated the investigation of individual influence of variation of these ensemble members on groundwater withdrawals over the 21st century.

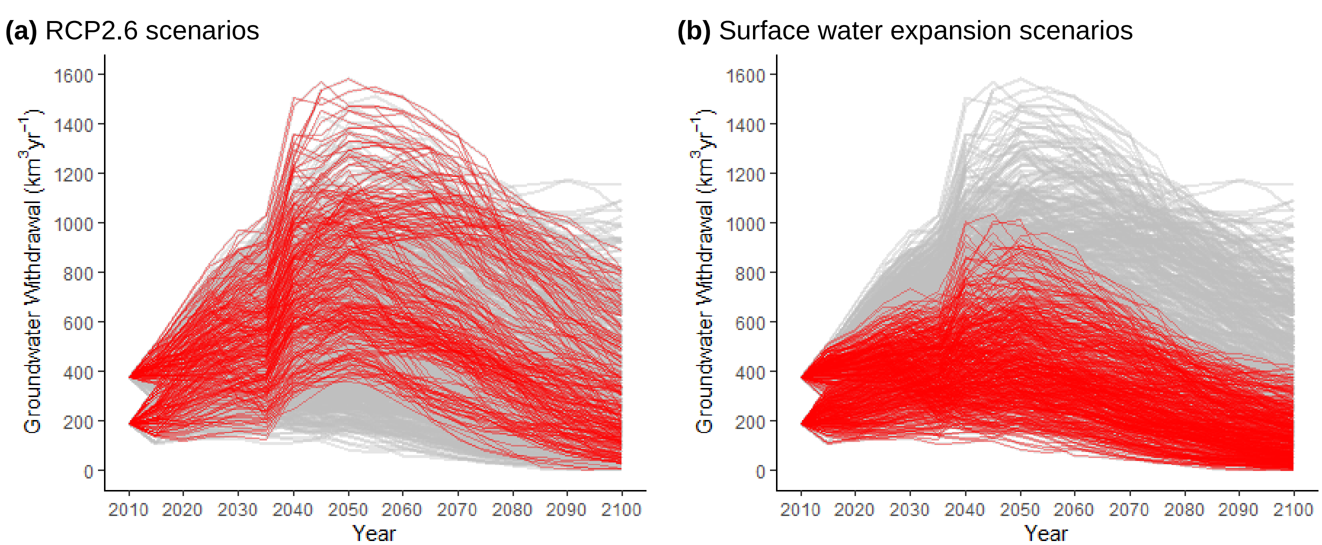

Fig. S11. Sensitivity of scenarios in **(a)** RCP2.6 **(b)** surface water expansion regimes for illustrative purposes.

Two of the variation categories in the experiment design, namely SSPs and RCPs, are widely known and studied by the community. Table S4 shows summary statistics (central and peak values) of global groundwater withdrawals and associated years by each feasible SSP and RCP combination.

Table S4. Summary statistics of global nonrenewable water withdrawals and associated year by each SSP and RCP combination.

SSP	RCP	Median Q	Median Yr	Mean Q	Mean Yr	Max Q	Max Yr
SSP1	RCP2.6	756.248	2050	792.95	2047.5	1239.389	2060
SSP1	RCP4.5	608.212	2037.5	636.481	2037	1001.61	2050
SSP1	RCP6.0	585.809	2030	616.122	2032.5	962.08	2045
SSP2	RCP2.6	750.671	2050	819.089	2051.5	1307.39	2070
SSP2	RCP4.5	631.037	2050	697.398	2048	1105.758	2070
SSP2	RCP6.0	603.292	2035	615.74	2038	996.406	2060
SSP3	RCP4.5	572.025	2055	652.202	2061.5	1180.801	2100
SSP3	RCP6.0	544.205	2037.5	589.849	2053	1033.071	2100
SSP4	RCP2.6	723.733	2050	764.464	2053	1206.221	2080
SSP4	RCP4.5	573.661	2050	603.958	2047	975.558	2065
SSP4	RCP6.0	492.638	2035	501.505	2036	845.954	2055
SSP5	RCP2.6	990.875	2050	1052.388	2048	1640.285	2055
SSP5	RCP4.5	899.811	2050	934.473	2051	1515.572	2060
SSP5	RCP6.0	678.501	2042.5	748.361	2041	1307.348	2065
SSP5	RCP8.5	652.014	2040	686.717	2039	1123.237	2050

Similarly, Fig. S12 shows the variation in global groundwater withdrawals according to each feasible combination of SSPs and RCPs. The width of the eclipse shows the strength of the dependence between peak groundwater withdrawal and peak year in an SSP-RCP combination, and the inclination of the eclipse shows the positive or negative nature of the dependence.

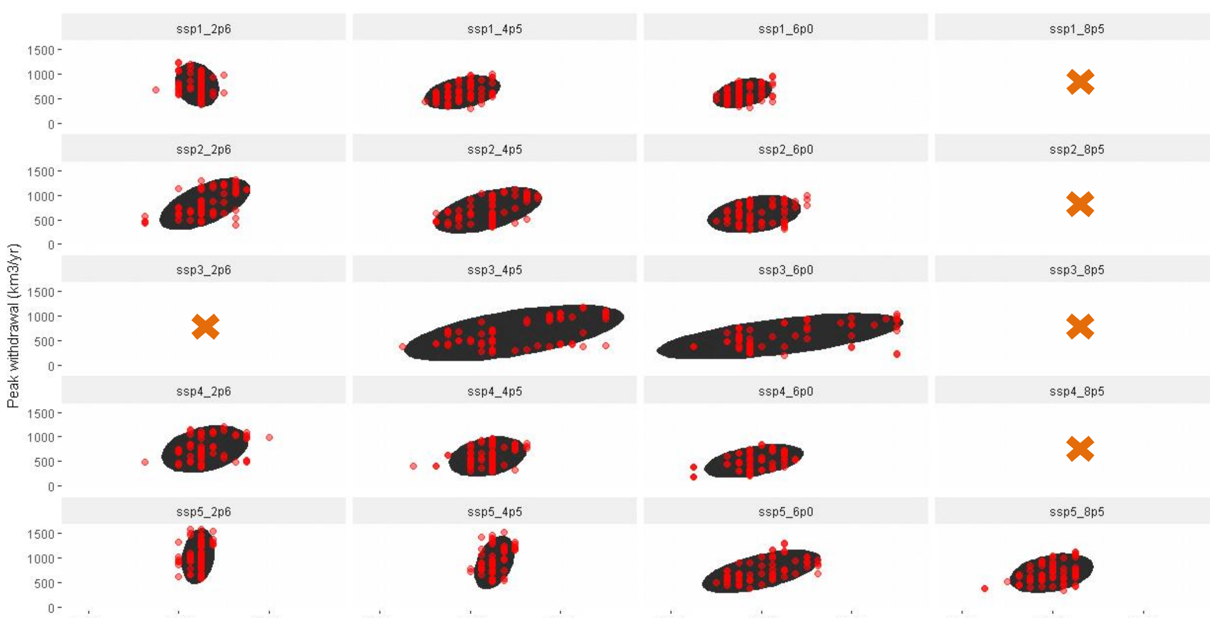

Fig. S12. Dependence eclipses of global peak nonrenewable water withdrawal and peak year for each feasible combination of SSP and RCP.

Sensitivity of Global Groundwater Withdrawals

As 900 GCAM scenarios were generated by combining variations across six parameter categories (Fig. S7), Fig. S13 shows relative frequency of occurrence for global groundwater withdrawals in year 2100 and cumulative groundwater withdrawals from 2010 till 2100 for each variation across the six parameter categories. The difference in relative frequency of variations in a category for a particular withdrawal value shows the relative contribution of each variation towards generating that particular withdrawal across all scenarios. Nearly all withdrawals patterns in 2100 are positively skewed towards smaller withdrawal magnitudes, whereas cumulative withdrawals show an asymmetric bimodal pattern.

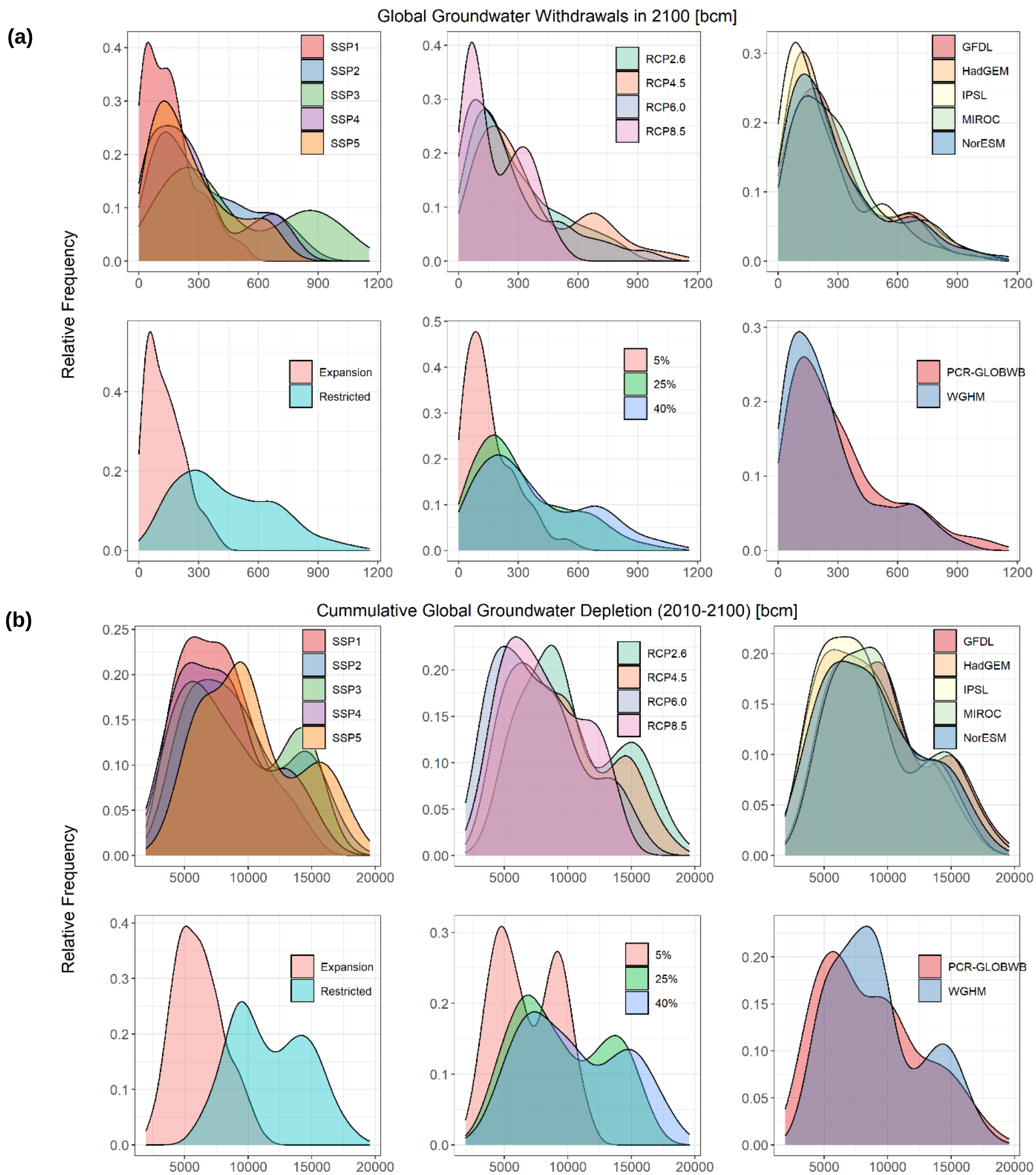

Fig. S13. Relative frequency of occurrence for (a) global groundwater withdrawals in year 2100 and (b) cumulative global groundwater withdrawals throughout the 21st century (2010-2100).

Peak Water Metrics

Table S5 shows the top ten GCAM regions, basins, and scenarios ranked by highest groundwater withdrawal from a total of 32 GCAM regions, 235 water basins, and 900 scenarios. For each peak withdrawal value in a particular category, corresponding details of other categories are also presented. For instance, basin Arabian Peninsula, which belongs to GCAM region Middle East, has the highest withdrawal in year 2065 in scenario *gl_hi_rs_ssp5_gfdl_2p6*.

Table S5. Top 10 GCAM regions, basins, and scenarios ranked by peak groundwater withdrawal.

Scenario*	GCAM region	GCAM basin	Peak year	Peak withdrawal (km^3 $year^{-1}$)
Peaks by GCAM regions				
gl_hi_rs_ssp5_gfdl_2p6	Middle East	Arabian Peninsula	2065	323.504
wg_hi_rs_ssp5_gfdl_2p6	China	Indus	2040	299.224
gl_hi_rs_ssp5_gfdl_2p6	Africa_Eastern	Nile	2095	263.617
gl_hi_ex_ssp1_gfdl_2p6	India	Sabarmati	2025	153.711
gl_hi_rs_ssp3_miro_4p5	Central Asia	Syr Darya	2090	101.913
gl_hi_rs_ssp5_miro_4p5	Europe_Non_EU	Tigris-Euphrates	2050	76.5392
gl_hi_rs_ssp5_ipsl_4p5	Africa_Northern	Mediterranean Sea-East Coast	2045	52.8001
wg_hi_rs_ssp3_miro_4p5	Brazil	La Plata	2100	43.7277
gl_hi_rs_ssp5_nrsm_4p5	USA	Rio Grande River	2095	43.4978
gl_hi_rs_ssp5_ipsl_8p5	Southeast Asia	Chao Phraya	2025	36.8183
Peaks by Water Basins				
gl_hi_rs_ssp5_gfdl_2p6	Middle East	Arabian Peninsula	2065	323.504
wg_hi_rs_ssp5_gfdl_2p6	China	Indus	2040	299.224
gl_hi_rs_ssp5_gfdl_2p6	Africa_Eastern	Nile	2095	263.617
wg_hi_rs_ssp1_gfdl_2p6	China	Ganges-Bramaputra	2050	161.322
gl_hi_ex_ssp1_gfdl_2p6	India	Sabarmati	2025	153.711
gl_hi_rs_ssp3_miro_4p5	Central Asia	Syr Darya	2090	101.913
gl_hi_rs_ssp5_miro_4p5	Middle East	Central Iran	2065	97.6401
gl_hi_rs_ssp4_miro_2p6	Central Asia	Caspian Sea-East Coast	2090	80.9728
gl_hi_rs_ssp5_miro_4p5	Europe_Non_EU	Tigris-Euphrates	2050	76.5392
gl_hi_ex_ssp3_gfdl_4p5	Central Asia	Amu Darya	2090	72.2637
Peaks by Scenarios				
gl_hi_rs_ssp5_gfdl_2p6	Middle East	Arabian Peninsula	2065	323.504
wg_hi_rs_ssp5_gfdl_2p6	Middle East	Arabian Peninsula	2065	322.149
gl_hi_rs_ssp5_ipsl_2p6	Middle East	Arabian Peninsula	2065	306.569
gl_hi_ex_ssp5_gfdl_2p6	Middle East	Arabian Peninsula	2065	305.544
wg_hi_rs_ssp5_ipsl_2p6	Middle East	Arabian Peninsula	2065	303.532
wg_hi_ex_ssp5_gfdl_2p6	China	Indus	2040	299.204
wg_hi_rs_ssp1_gfdl_2p6	Middle East	Arabian Peninsula	2065	296.357
wg_hi_ex_ssp1_miro_2p6	China	Indus	2040	294.876
gl_hi_rs_ssp1_gfdl_2p6	Middle East	Arabian Peninsula	2065	294.854
wg_hi_rs_ssp1_miro_2p6	China	Indus	2040	294.69

***** Read scenarios as *gl* = PCR-GLOBWR calibration data, *wg* = WGHM calibration data; *hi* = 40% groundwater depletion limit; *rs* = restricted/no surface water storage growth, *ex* = surface water storage expansion; *SSP1-5* = shared socioeconomic pathways; *gfdl /miro /ipsl* = climate models; and *2p6 /4p5 /8p5* = representative concentration pathways (RCPs) 2.6, 4.5, and 8.5.

Global maps in Fig. S14 show different peak water metrics relevant for providing a better understanding of the broader withdrawal dynamics for each basin. These figures question the probability of occurrence of peak-and-decline for a basin across multiple scenarios and the associated metrics to know if the peak-and-decline is affecting the basin dynamics. For instance, if a basin experiences peak-and-decline, Fig. 13b-e questions when does each basin peak and what's the median depletion for that year, what is the ratio of nonrenewable water withdrawal to total water withdrawals, and associated cost of extracting that water. Superimposing the plots can reveal critical hotspots of nonrenewable water withdrawals over the 21st century.

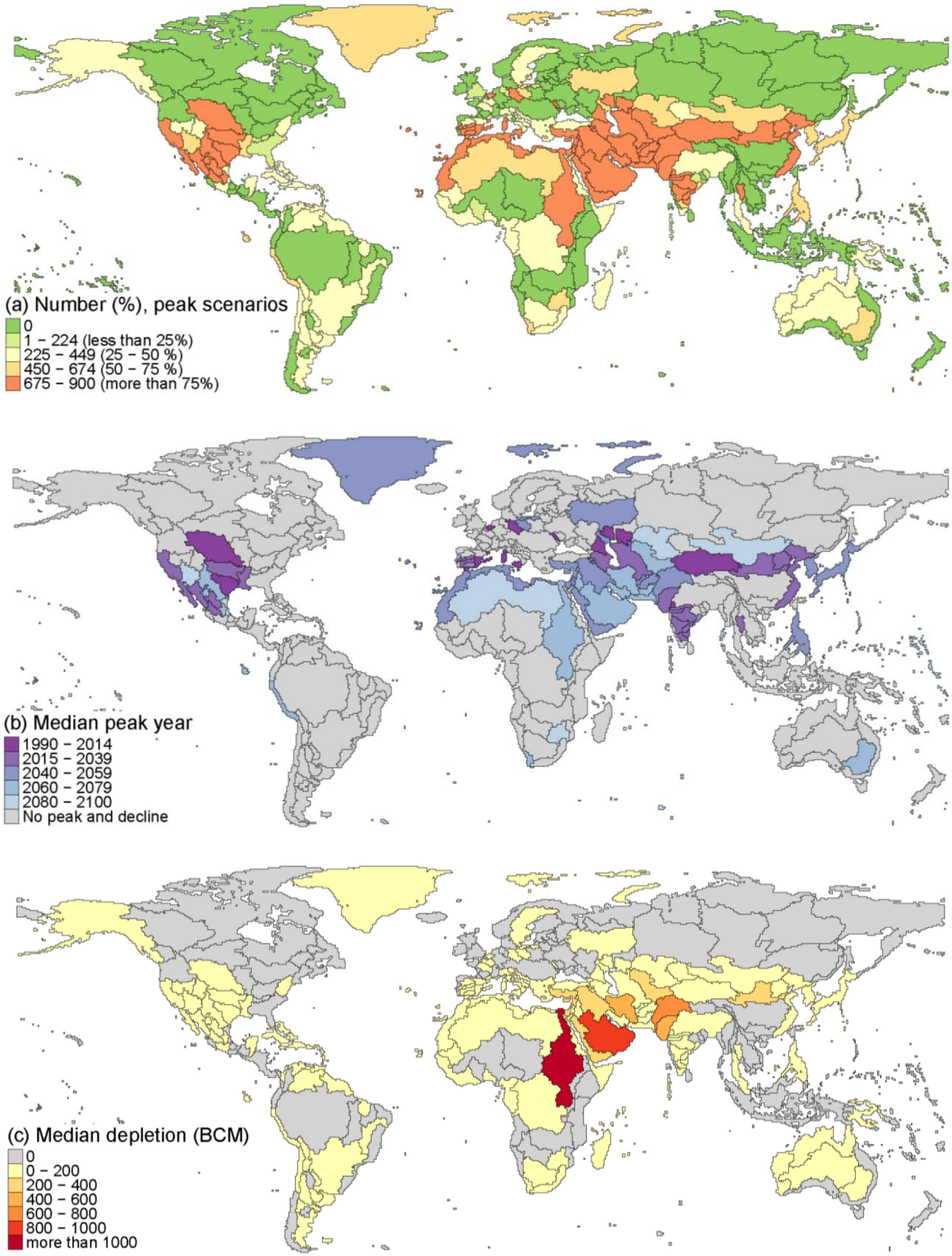

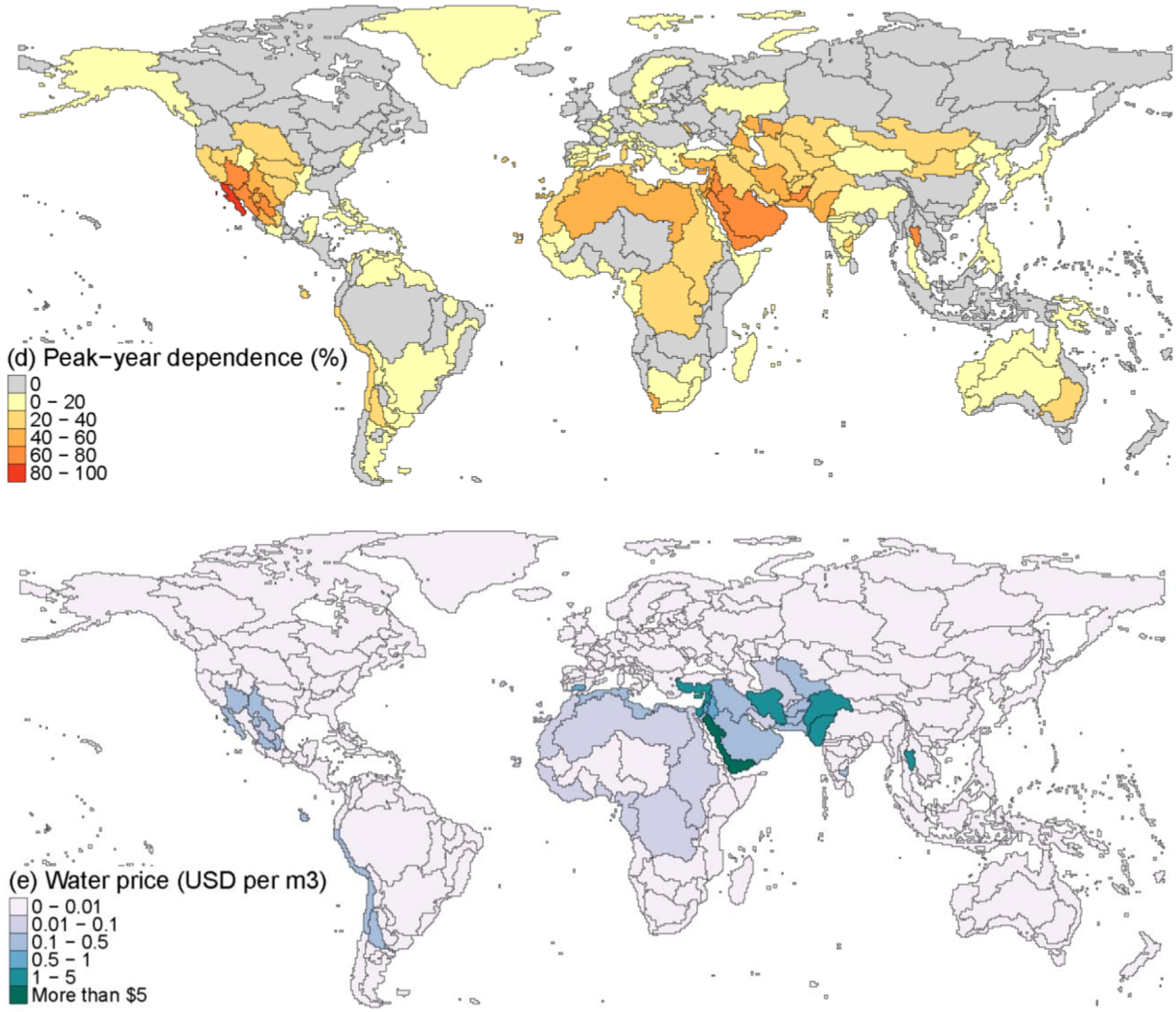

Fig. S14. Set of global maps showing various basins according to the (a) number of scenarios in which groundwater withdrawals peak and decline, (b) median peak year across all scenarios, (c) median groundwater depletion rate for the peak year, (d) median groundwater dependence as a proportion of conventional water for the peak year, and (e) water prices per cubic meter of groundwater extraction.

Table S6. List of basins that may have already peaked before 2023. Median peak year and fraction of scenarios in which a basin might have peaked are also presented.

GCAM Basin ID	GCAM Basin Name	Fraction of scenarios in which this basin peaked	Median Peak Year
45	Caspian Sea-East Coast	0.92	1990
49	Dniester	1.00	1990
31	Elbe	0.91	2005
63	Mediterranean Sea-East Coast	0.93	2005
36	Scheldt	0.96	2005
67	Spain-South and East Coast	0.89	2005
225	Texas Gulf Coast	0.87	2005
113	Mahi	1.00	2010
223	Missouri River	0.94	2010
85	Tarim Interior	0.89	2010
224	Arkansas White Red	0.94	2015
217	California River	0.98	2015
78	China Coast	1.00	2015
235	Narmada	1.00	2015
147	Pennar	0.99	2015
117	Tapti	0.99	2015
72	Caspian Sea Coast	1.00	2020
123	Godavari	0.88	2020
81	Guadiana	0.95	2020
145	India East Coast	0.98	2020
96	Mexico-Northwest Coast	0.96	2022.5

Multisector Exposure to Groundwater Peak-and-Decline

Population Vulnerability

Groundwater dynamics actively interact with the integrated human-earth system in multiple ways and forms. Human water demands in domestic, municipal, industrial, and agricultural sectors tend to affect the magnitude of groundwater withdrawals. This interaction suggests that if economically accessible volume of groundwater where to become limited, this scarcity is going to have a profound effect on human well-being.

Our results suggest the on average 44.1% of global population i.e., 3.2 billion today, will experience peak-and-decline based groundwater stress over the 21st century. Fig. S15 shows the fraction of global population living in groundwater basins that will experience peak and decline over the 21st century. Nearly half of the global population being exposed to groundwater peak-and-decline signals the vulnerability of society to limited water resources underground. This will vulnerability is not expected to be confined to water resources but would likely trickle down to other systems, such as food and agriculture, which are essential for smooth functioning of the society.

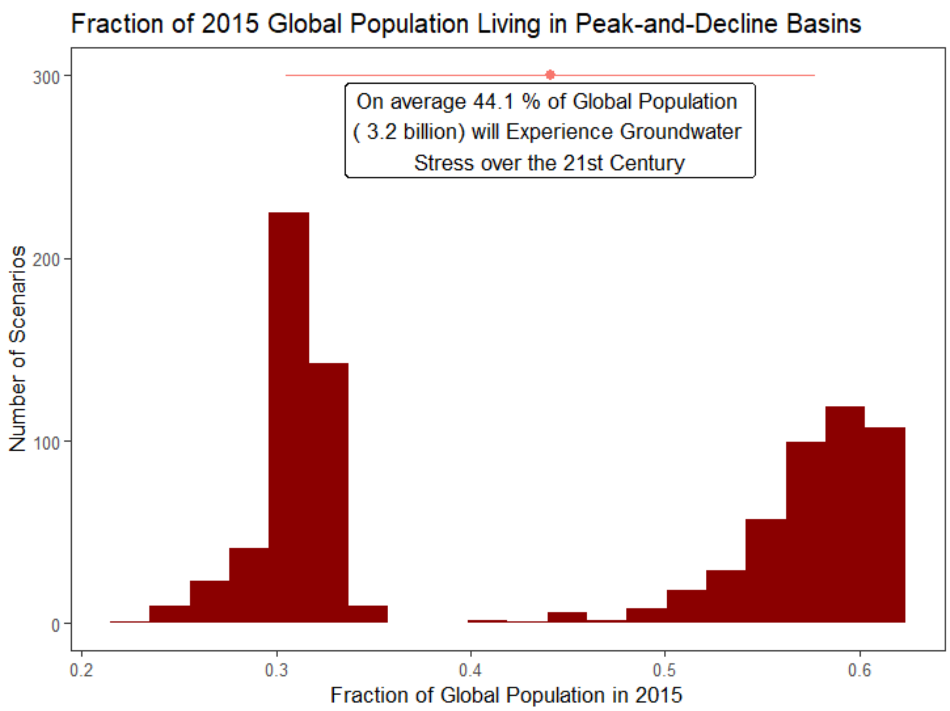

Fig. S15. Fraction of global population in 2015 living in basins that will face peak groundwater depletion over the 21st century. On average 44.1% of global population (3.2 billion in 2015) will undergo groundwater stress over the 21st century.

Along with a wide range of population fraction exposed to groundwater peak-and-decline, one noteworthy feature of Fig. S15 is the bi-modal shape of the histogram concentrated around 30% on the lower end and 60% on the higher end of the fractions of the global population. This bi-modal feature is hypothesized to be sensitive to the experimental design, meaning that some variations in the ensemble members is causing only small and less water intensive basins, with low population footprint to peak, whereas other variation of the ensemble members is causing large, highly water intensive, with high population basins to peak. This also suggests that this bi-modal feature could also be driven by the characteristics of the underlying basins, including their water supply sources, water consumption patterns, and the population magnitude in those regions. The basins on the lower fraction side of the histogram are small with low population but also have scarce surface and groundwater supply. Contrarily, the basins on the higher side of the fraction are large population intensive and major food producers.

Agricultural Sector Exposure

The adoption of groundwater irrigation at a massive scale has allowed for massive arable lands that are not viable for rainfed production to enter into agriculture production. Running out of economically extractable fresh groundwater could have a profound impact on the geography of international trade, especially agriculture given the large dependence of current agricultural productions on groundwater resources. Fig. S16 shows fraction of global agricultural production in water basins that will experience a peak-and-decline in groundwater depletion over the 21st century. The results suggest that 40%±13% of global agricultural production and 35%±10% of global biomass production in 2100 occurs in water basins that will experience a peak and decline in their dependence on non-renewable groundwater resources over the 21st century.

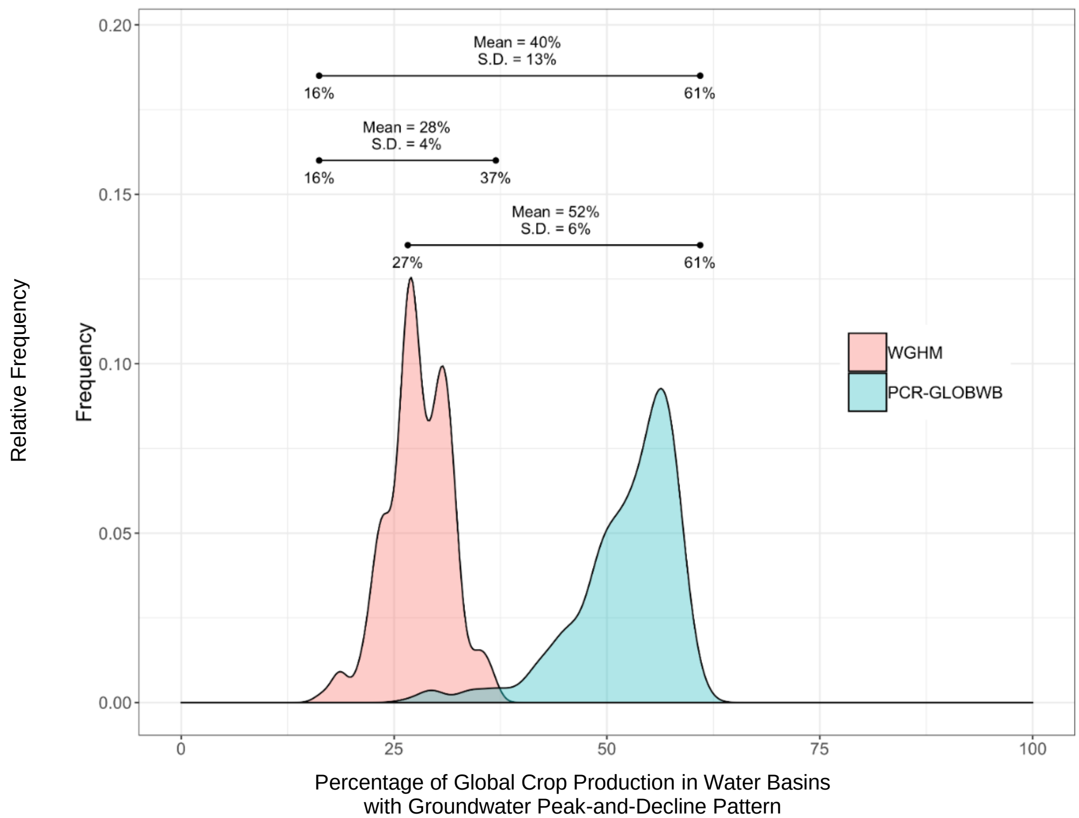

Fig. S16. Fraction of global agricultural production in year 2100 in water basins that will experience a peak and decline in groundwater withdrawals over the 21st century.

Accurate investigation of sensitivity of peak dynamics to ensemble variables through formal scenario discovery techniques would uncover the exact cause of variations in output metrics. Such preliminary analysis and commentary are presented in the following sections of the SI.

Drivers of Groundwater Peak Dynamics

Uncertainty in Ensembles

Fig. S17 shows the stylized methodology used to generate peak metrics. Each peak-and-decline scenario has a peak withdrawal and a peak year. These data points are collected and relevant metrics are calculated to better understand the sensitivity of peak dynamics and uncertainty in outputs with respect to variations in ensemble members of the experiment design.

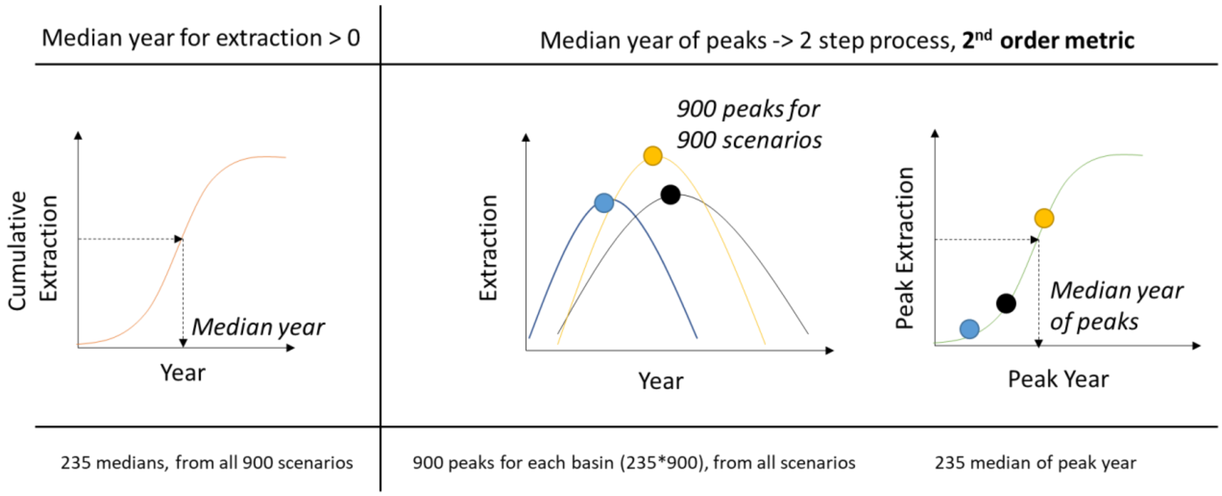

Fig. S17. Stylized methodology for calculating peak metrics from 900 scenarios

Understating uncertainty in peak groundwater withdrawals and peak year is vital to understand which drivers cause more significant variations in peaks than others. Fig. S18 shows the sensitivity and uncertainty in peak withdrawals and peak year across all ensemble members of the experimental design. The violins show the uncertainty in peak groundwater withdrawals, symmetrically mirrored across median peak year, in the respective panel of each ensemble member. For interpretation, wider the violins, more the frequency of results (peak withdrawals) around that value on vertical axis.

(a) shared socioeconomic pathways

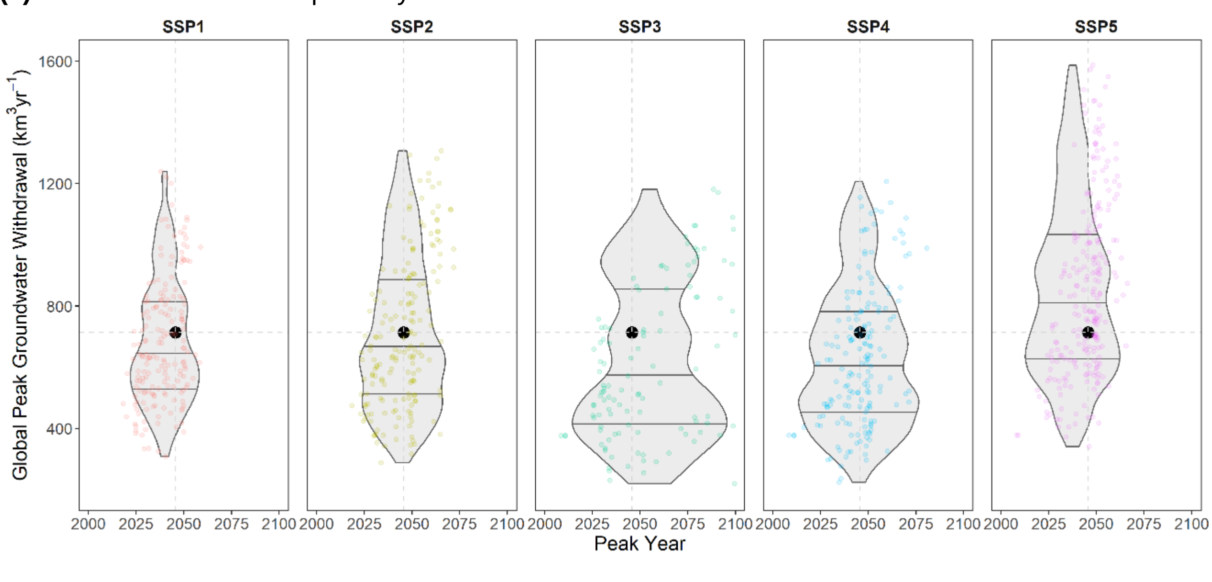

(b) Representative conceptarion pathways

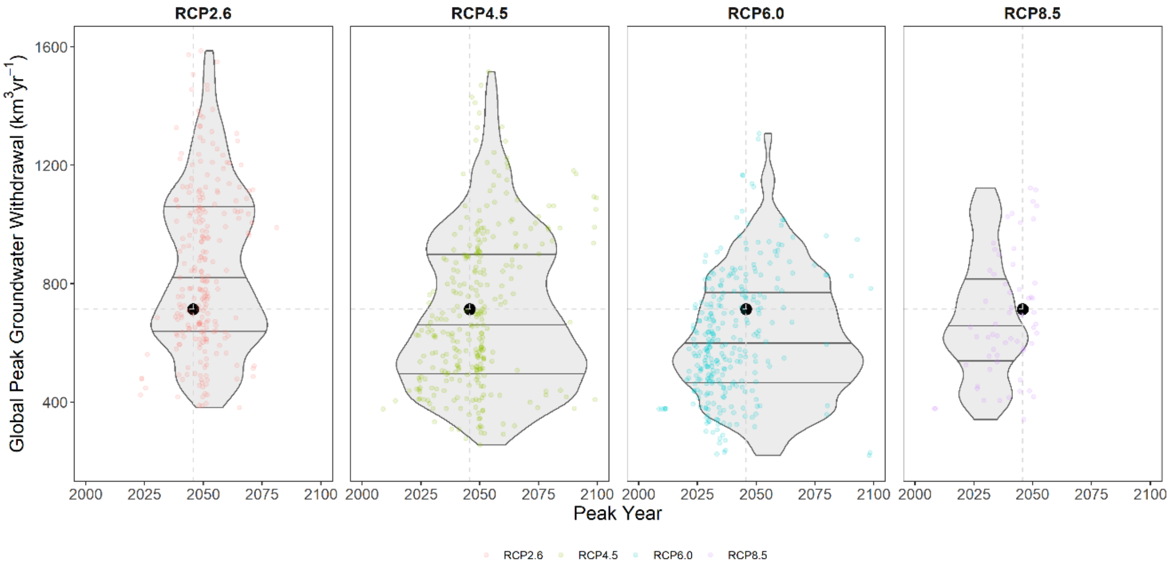

(c) grounwdater depletion limits sceanrios

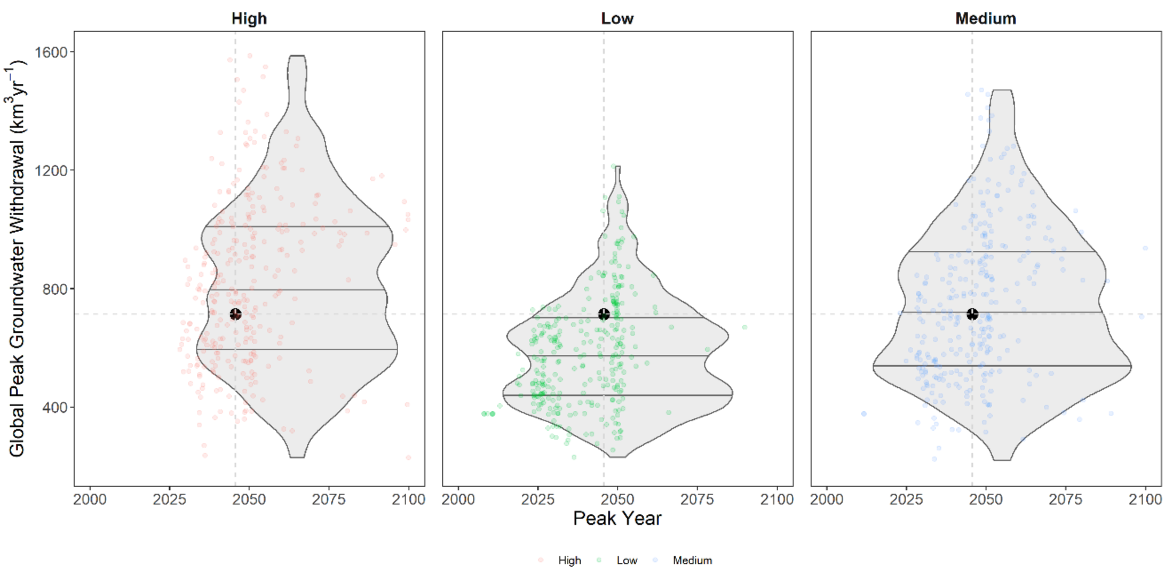

(d) climate impact models

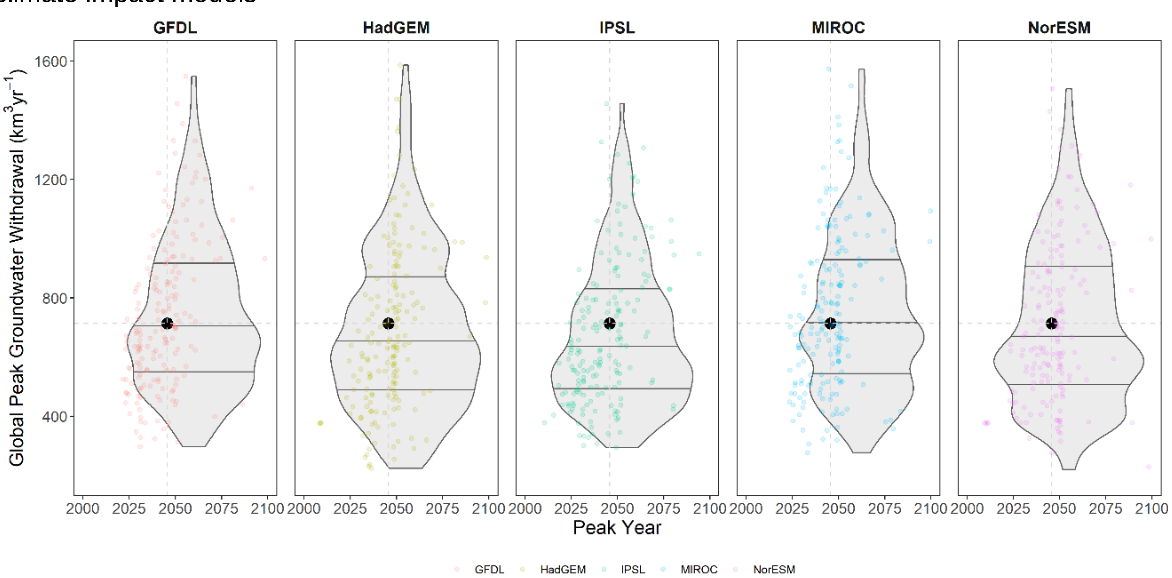

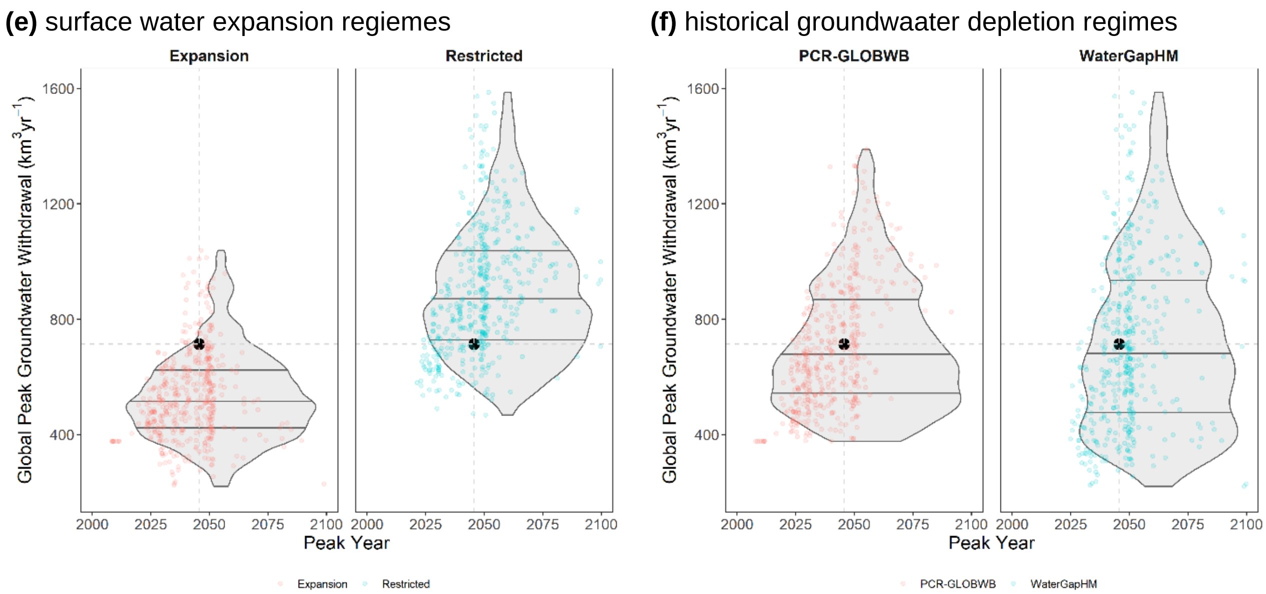

Fig. S18. Sensitivity of peak water and peak year according to each ensemble member in experiment design. Violin plots are symmetric probability distributions across vertical axis. In this context these show relative frequency of peak withdrawals according to a peak year. Colored dots are individual peak withdrawal and peak year realizations for each of the scenario in a particular variation of the ensemble member. The three horizontal lines show quartiles. The black dot shows global median across all scenarios and can be used to compare the deviation of outcomes for each ensemble member.

Individual Variable Sensitivity Comparisons

Sensitivity of peak metrics to individual variables is highlighted in Fig. S19 which shows probability distributions and in Fig. S20 which shows cumulative probability distributions for both peak groundwater withdrawals and peak year according to each ensemble member of the experimental design. The maximum relative deviation among each of the probability distribution plots represent the sensitivity of peak metrics to the variation in the ensemble member.

In other words, output of the runs is considered sensitive to parameters if probability densities plots don't align well. For instance, future surface water storage drives a clear distinction between probability density of peak withdrawals under expanded and restrictive regimes. This means that future trends in groundwater withdrawals are sensitive to the degree of investment in surface water storage expansion infrastructure. Similarly, the probability distribution of peak year under scenarios with RCP2.6 is considerably different from the probability distributions of peak year under other RCPs. This suggests that the timing of peak groundwater withdrawals over the 21st century is going to be sensitive to climate mitigation efforts, GHG emissions in atmosphere, and overall radiative forcing under which hydrological systems have to operate.

Similar trends of variability and sensitivity to ensemble members in the scenarios are also observed in cumulative probability distribution of peak metrics in Fig. S20. For instance, cumulative distribution of peak year in SSP3 scenario starts to deviate considerably from other SSPS after mid-century. This is due to the unique underlying population and technological trends consistent with SSP3 narrative, in which population grows throughout the century and a lack of investments in technological change to increase water use efficiencies in end-use sectors is observed.

Based on comparison across all parameter categories, we notice that supply-side drivers (reservoir storage & groundwater restrictions) impact peak withdrawal magnitude the most, while demand-side drivers (RCPs & SSPs) impact peak timing.

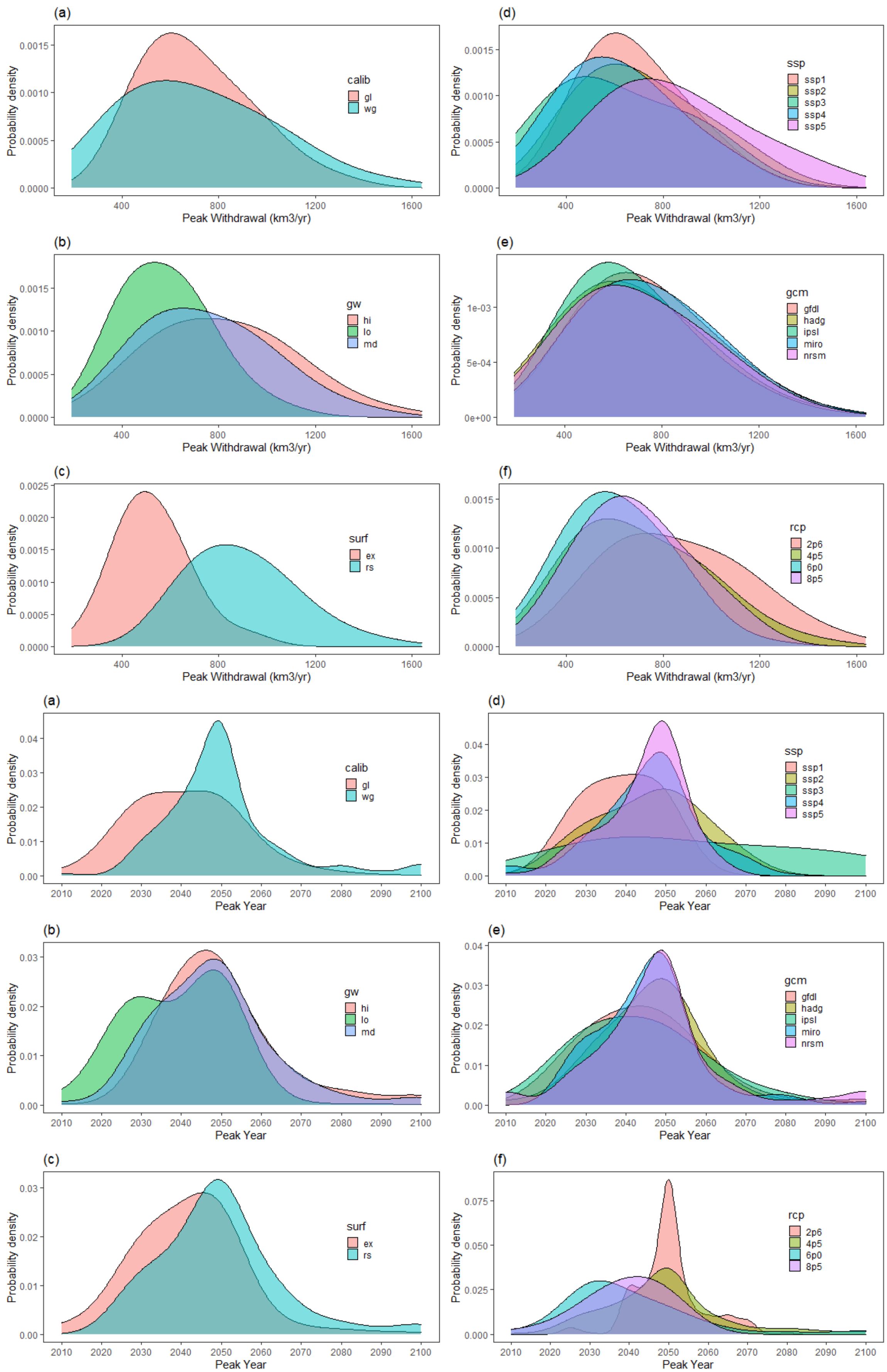

Fig. S19. Probability distributions of peak withdrawals (top 6) and peak year (bottom 6) under scenarios where only the respective ensemble member colored in each panel was varied.

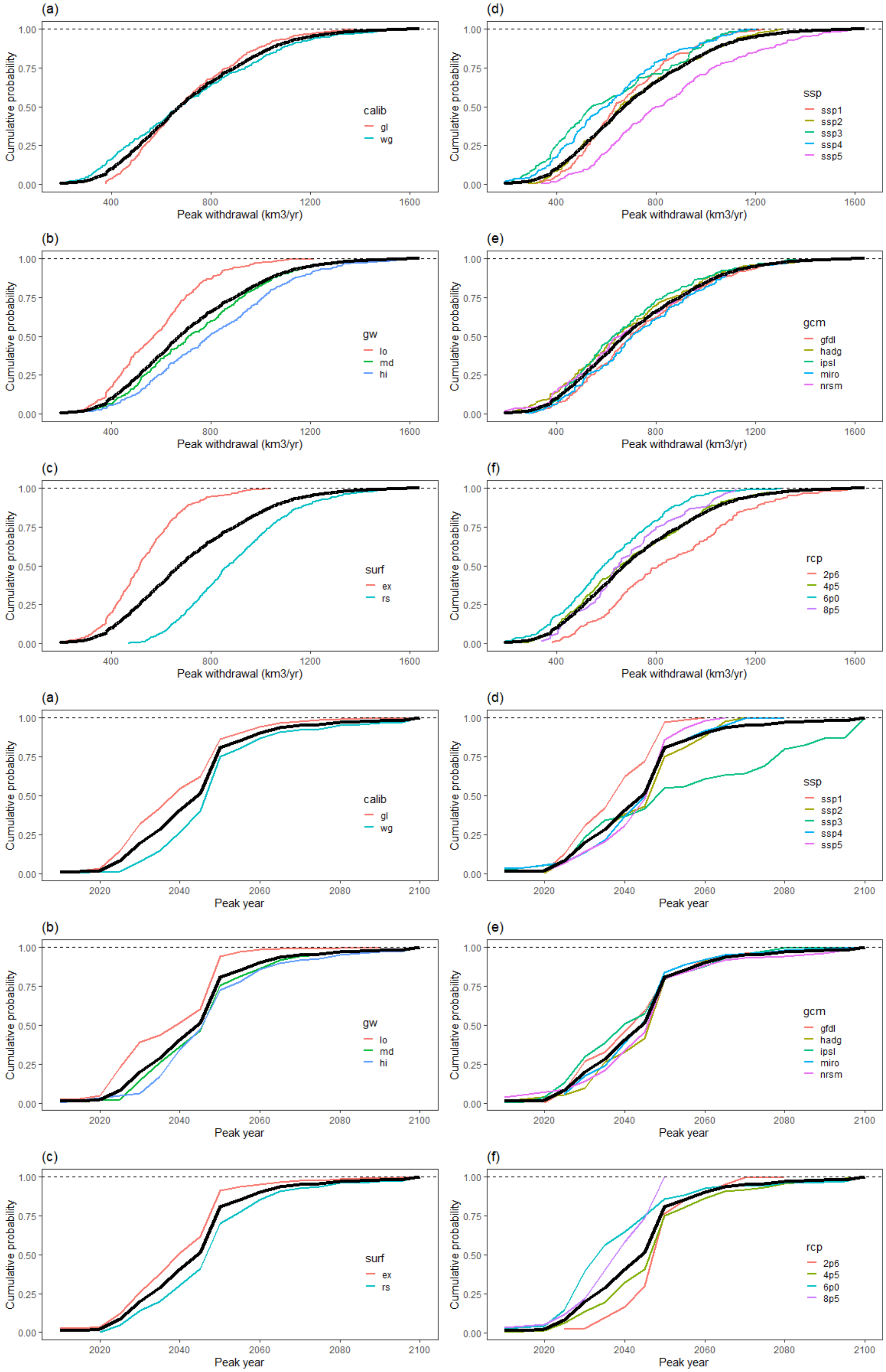

Fig. S20. Cumulative probability distributions of peak withdrawals (top 6) and peak year (bottom 6) under scenarios where only the respective ensemble member colored in each panel was varied.

Dependence Structure

Along with understanding uncertainty in outputs due to individual ensemble members, the interconnection and dependence of all ensemble members among each other and on peak metrics was also analyzed. In reality most of the drivers of global change could be connected to each other, and due to these interconnections, they might offer a collective influence towards causing variations in outcomes. In case of two positively reinforcing influencing factors, if also happen to be positively correlated, can have an 'amplified' influence on the outcome and can cause nonlinear shifts in dynamics of the outcome. The motivation behind dependence analysis was to investigate inter-variable connections among both influencing variables (ensemble members of the experimental design) and the outcomes of the experiment (peak metrics) to understand compounding influences on peak metrics and reveal the hidden interdependencies which might not have been recognizable through one-to-one uncertainty mapping from variables to outcomes.

Among many ways to understand the dependence structures, we have used nonparametric Bayesian networks (NPBN) as shown in Fig. S21. NPBNs are a form of Bayesian networks which can incorporate both discrete and continuous data in one network (Hanea et al., 2015). Bayesian networks have roots in multivariate probability theory and graph theory, where the former is used to calculate inter-variable dependence and the latter is used to display it in a relatively simpler manner. The anatomical structure of a Bayesian network contains nodes and arcs where nodes represent variables in the form of marginal distributions and arcs represent dependencies in the form of rank correlations. These nodes and arcs form a directed acyclic graph which makes representing conditional dependence possible. Nonparametric Bayesian networks are based on copulas, specifically Gaussian copula, which utilize ranks of the data, rather than the actual values, to capture the dependence structure so that if the absolute range of the parameter values changes the dependence structure could be utilized to resample from the copula for the new value range (Niazi, 2019; Niazi et al., 2021). Eventually NPBNs represent a copula-based large consistent joint probability distribution of all variables in the Bayesian network. A few of the key advantages of NPBNs is their ability to handle large amounts of data, ability to handle missing data, and to adapt the structure of the network to the data.

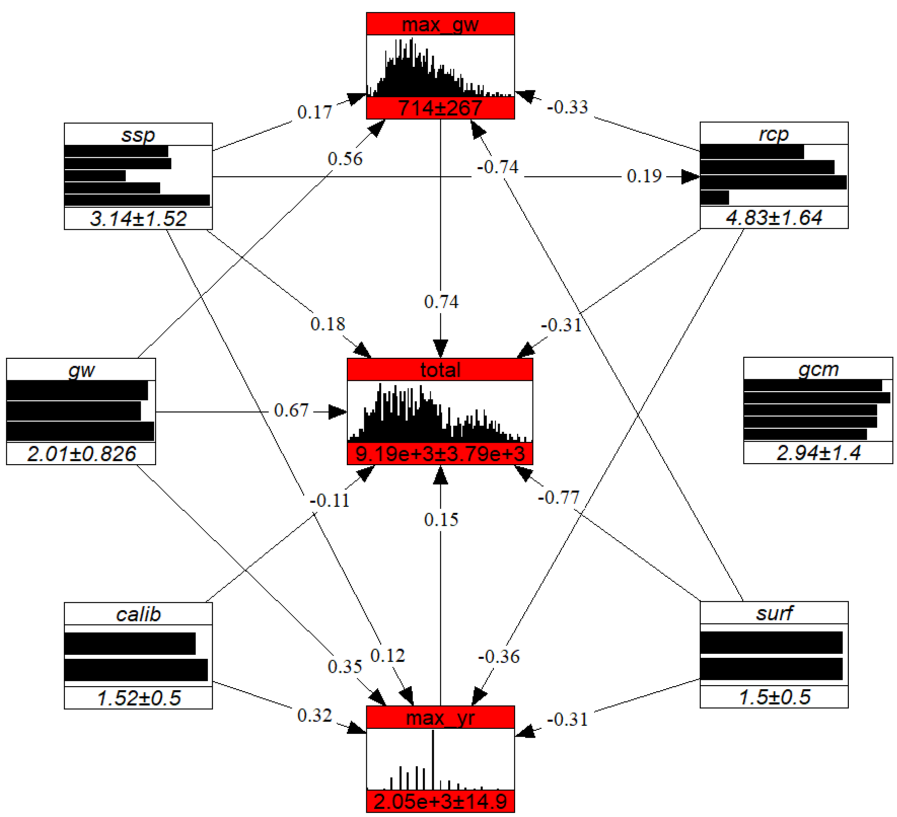

Fig. S21. Nonparametric Bayesian network showing interconnections among ensemble members (black boxes) and peak metrics (red boxes). The bars on nodes are marginal distributions and the numbers on arcs are rank correlations. *max_gw* represents peak withdrawal, *total* represents total withdrawals over 21st century, and *max_yr* represents peak year. All influencing variables were converted to discrete identifiers which means the mean and standard deviation at the bottom of each parameter's box are not actual values but only represent the identifier. The identifiers represent following realizations: *SSPs*: 1-5; *RCPs* 1-4 = 2.6, 4.5, 6.0, 8.5; *Calib*: gl=1, wg=2; *surf*: 1=ex, 2=rs; *gw*: lo=1, md=2, hi=3; and *GCMs*: 1-5 = GFDL, HadGEM, IPSL, MIROC, NorESM.

Fig. S21 shows a nonparametric Bayesian network of influencing factors and peak metrics. Arcs with relatively less important correlations, i.e., less than 0.1, were removed to make the network unsaturated, while still being able to capture the dependence structure as that of a fully saturated network, in which everything is connected to everything. We observe that peak groundwater withdrawals seem to be positively correlated with total withdrawals over the 21st century, which means basins that are extracting heavily over a short period of time are also the basins that are extracting a lot over the century. This is a matter of concern not only for the future resource evolution of groundwater but also for the groundwater-influenced multisector dynamics associated with, for example, agricultural productivity and associated global food flows along with associated well-being of the population living in these peak-and-decline basins. Another important feature that emerges out of this exercise is the disconnect between peak groundwater withdrawals and peak year, which suggests that there is a wide variety of time windows in which water basins are expected to peak, and the peak-and-decline induced water stress is going to shift from regions over time. Making these make hidden interdependencies explicit allows us to better understand and plan adaptation strategies under these interconnected peak dynamics.

Table S6 shows the correlation matrix of all correlations among influencing factors (ensemble members of the experimental design) and peak metrics along with total groundwater withdrawals. We note that due to uniform sampling of all ensemble members, where every variable was varied individually in a scenario, and was combined with all other variables to capture the full parameter space, there is no dominant correlation among the influencing factors/ensemble members, with the exception of SSPs and RCPs because of the combinatorial constraints among socioeconomic development and radiative forcing as explained in Fig. S7.

Table S7. Correlation matrix of all ensemble members in the experimental design and the resulting peak metrics.

	SSP	**RCP**	**GCM**	**CalibData**	**Storage**	**GWlimits**	**PeakYear**	**PeakWater**	**Total**
SSP	1	0.19	0	0	0	0	0.12	0.17	0.18
RCP	0.19	1	0	0	0	0	-0.32	-0.28	-0.26
GCM	0	0	1	0	0	0	0	0	0
CalibData	0	0	0	1	0	0	0.30	0	-0.11
Storage	0	0	0	0	1	0	-0.27	-0.68	-0.71
GWlimits	0	0	0	0	0	1	0.29	0.34	0.38
PeakYear	0.12	-0.32	0	0.30	-0.27	0.29	1	0.43	0.46
PeakWater	0.17	-0.28	0	0	-0.68	0.34	0.43	1	0.93
Total	0.18	-0.26	0	-0.11	-0.71	0.38	0.46	0.93	1

Regarding peak metrics, we observe that peak year has the highest dependence on RCPs, which means that the level of radiative forcing as a result of decarbonization and climate mitigation efforts is going to have the most significant influence on when groundwater withdrawals peak. Similarly peak groundwater withdrawals have maximum dependence on surface water storage expansion regimes, which means that the degree to which we invest in surface water infrastructure is going to determine the dynamics associated with groundwater withdrawals over the 21st century. Surface water expansion regimes not only have the strongest influence on peak groundwater withdrawals, but they also most significantly affect total groundwater withdrawals over the 21st century. This calls for increased efforts on understanding and intentionally mainstreaming the interface between surface water storage and groundwater withdrawal dynamics for research, infrastructure planning, and policymaking. (von Lampe et al., 2014)

Spatial Boundaries in GCAM

This section includes spatial delineations of sectoral scales globally that dynamically interact to produce consistent energy-water-land nexus dynamics over time.

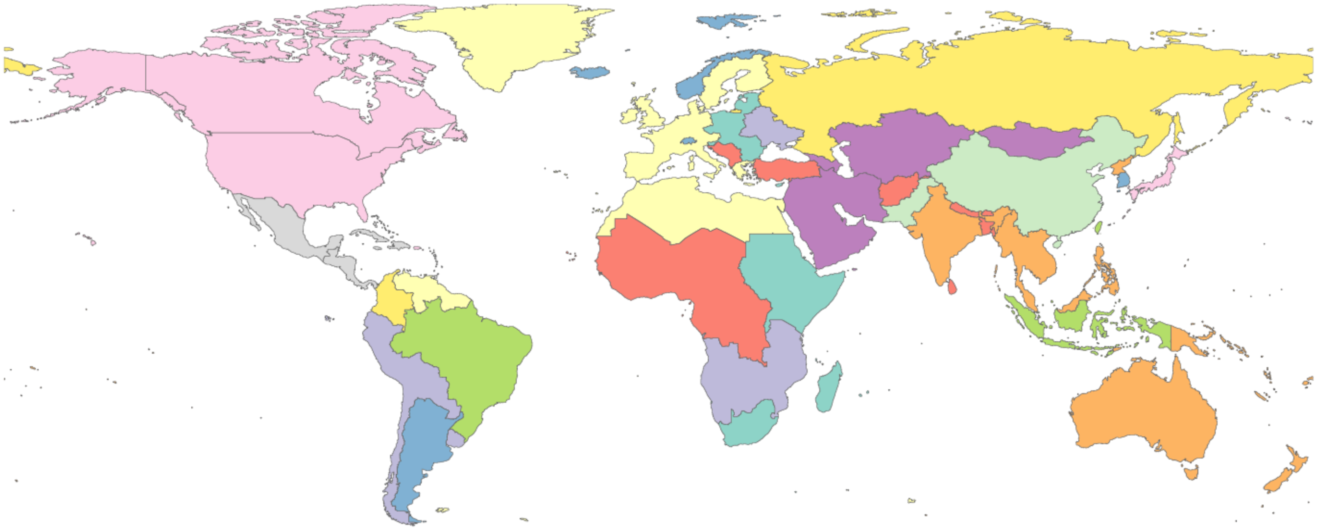

Fig. S22. GCAM 32 Energy-Economy Regions

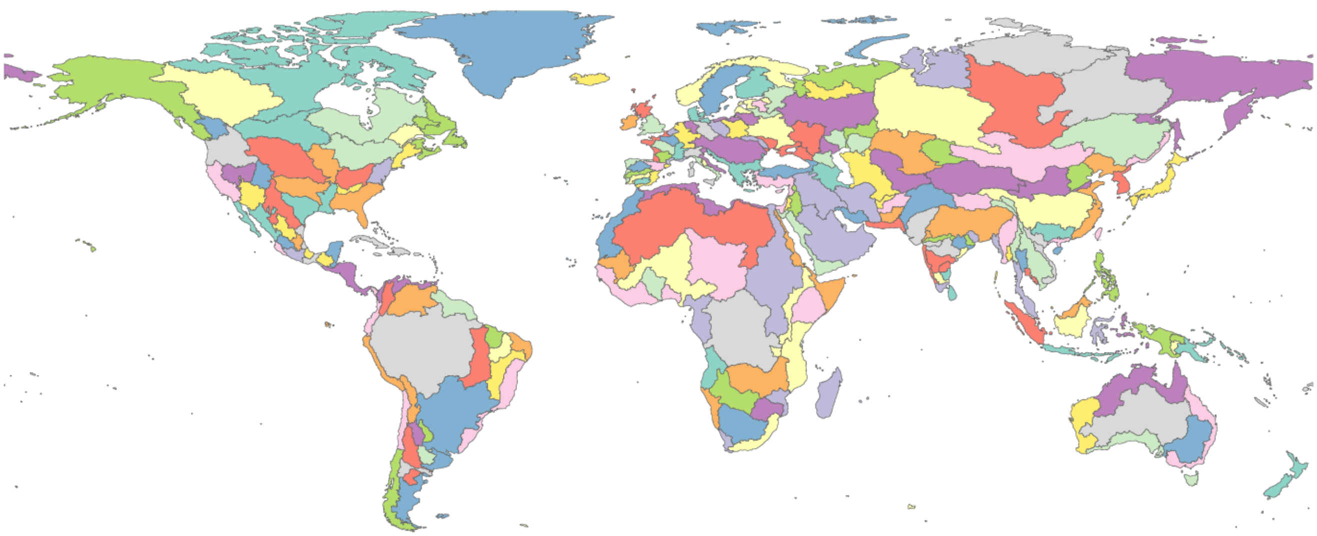

Fig. S23. GCAM 235 Water Basins

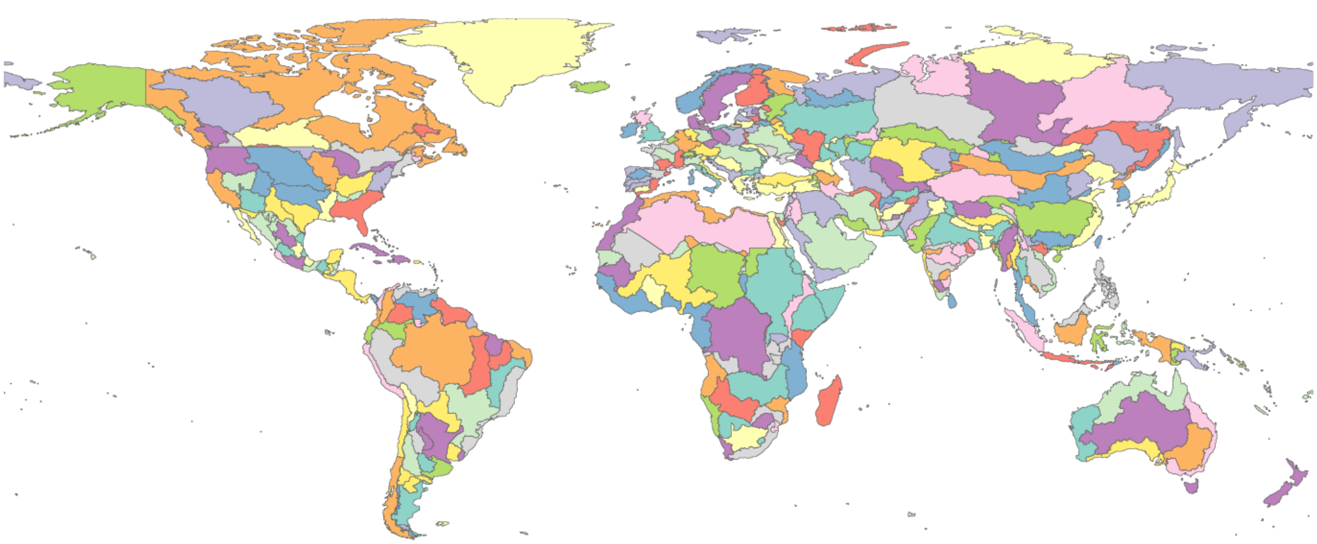

Fig. S24. GCAM Land Units

Meta-repository for Open Science

A meta-repository of this work is hosted on GitHub and Zenodo where all data and code used to setup, analyze, and post-process the simulations is made public adhering to open science best practices for reproducibility and transparency. Access the data and code by following the links:

- Meta-repository:
  - On github: https://github.com/JGCRI/niazi-etal_2024_nature-sustainability,
  - Minted version of the repository: https://zenodo.org/badge/latestdoi/658384847
- Large ensemble dataset on Zenodo: https://doi.org/10.5281/zenodo.6480465. The dataset contains:
  - GCAM executable
  - input *xmls* used to run GCAM simulations
  - consolidated output of the 900 model runs
  - post-processed model outputs in *.csv* format
  - scripts used for analysis and plotting figures
  - analysis output tables

Table S8. Structure and major contents of the meta-repository associated with this study.

Item	Purpose	Key folders and files
model/	Contains data and scripts required for reproducing the experiment ranging from steps related to setting up the model to running batch simulations to querying relevant outputs from 900 GCAM runs	water-data/, combined_impacts/, xml-creation/, xml-batch/, config_files/, gcam-5/, batch-scripts/, queries/, and outputs/ folders
processing/	Contains scripts and files required to reproduce the analysis and visualizations as presented in the paper	inputs/ and ouputs/ folders along with *.R scripts for analysis
figures/	Contains major figures presented in the manuscript	figures and shape files to plot maps
data	Associated data repository to host larger files and folders. This code repository must be complemented with data from data repository	https://doi.org/10.5281/zenodo.6480465

References

Abbott, B. W., Bishop, K., Zarnetske, J. P., Minaudo, C., Chapin, F. S., Krause, S., Hannah, D. M., Conner, L., Ellison, D., Godsey, S. E., Plont, S., Marçais, J., Kolbe, T., Huebner, A., Frei, R. J., Hampton, T., Gu, S., Buhman, M., Sara Sayedi, S., . . . Pinay, G. (2019). Human domination of the global water cycle absent from depictions and perceptions. *Nature Geoscience*, *12*(7), 533-540. https://doi.org/10.1038/s41561-019-0374-y

Birnbaum, A., Lamontagne, J., Wild, T., Dolan, F., & Yarlagadda, B. (2022). Drivers of Future Physical Water Scarcity and Its Economic Impacts in Latin America and the Caribbean. *Earth's Future*, *10*(8), e2022EF002764. https://doi.org/10.1029/2022EF002764

Bond-Lamberty, B., Dorheim, K., Cui, R., Horowitz, R., Snyder, A., Calvin, K., Feng, L., Hoesly, R., Horing, J., Kyle, G. P., Link, R., Patel, P., Roney, C., Staniszewski, A., Turner, S., Chen, M., Feijoo, F., Hartin, C., Hejazi, M., & Iyer, G. (2019). gcamdata: An R Package for Preparation, Synthesis, and Tracking of Input Data for the GCAM Integrated Human-Earth Systems Model. *Journal of Open Research Software*, *7*(1). https://doi.org/10.5334/jors.232

Bruinsma, J. (2009). *The Resource Outlook To 2050 : By How Much Do Land, Water And Crop Yields Need To Increase By 2050?* (Expert Meeting on How to Feed the World in 2050, Issue. https://cir.nii.ac.jp/crid/1571135650782357248

Calvin, K., Patel, P., Clarke, L., Asrar, G., Bond-Lamberty, B., Cui, R. Y., Di Vittorio, A., Dorheim, K., Edmonds, J., Hartin, C., Hejazi, M., Horowitz, R., Iyer, G., Kyle, P., Kim, S., Link, R., McJeon, H., Smith, S. J., Snyder, A., . . . Wise, M. (2019). GCAM v5.1: representing the linkages between energy, water, land, climate, and economic systems. *Geosci. Model Dev.*, *12*(2), 677-698. https://doi.org/10.5194/gmd-12-677-2019

Chaturvedi, V., Hejazi, M., Edmonds, J., Clarke, L., Kyle, P., Davies, E., & Wise, M. (2015). Climate mitigation policy implications for global irrigation water demand. *Mitigation and Adaptation Strategies for Global Change*, *20*(3), 389-407. https://doi.org/10.1007/s11027-013-9497-4

Dalin, C., Wada, Y., Kastner, T., & Puma, M. J. (2017). Groundwater depletion embedded in international food trade. *Nature*, *543*(7647), 700-704. https://doi.org/10.1038/nature21403

de Graaf, I. E. M., Sutanudjaja, E. H., van Beek, L. P. H., & Bierkens, M. F. P. (2015). A high-resolution global-scale groundwater model. *Hydrol. Earth Syst. Sci.*, *19*(2), 823-837. https://doi.org/10.5194/hess-19-823-2015

de Graaf, I. E. M., van Beek, R. L. P. H., Gleeson, T., Moosdorf, N., Schmitz, O., Sutanudjaja, E. H., & Bierkens, M. F. P. (2017). A global-scale two-layer transient groundwater model: Development and application to groundwater depletion. *Advances in Water Resources*, *102*, 53-67. https://doi.org/10.1016/j.advwatres.2017.01.011

Dolan, F., Lamontagne, J., Link, R., Hejazi, M., Reed, P., & Edmonds, J. (2021). Evaluating the economic impact of water scarcity in a changing world. *Nature Communications*, *12*(1), 1915. https://doi.org/10.1038/s41467-021-22194-0

Döll, P., Müller Schmied, H., Schuh, C., Portmann, F. T., & Eicker, A. (2014). Global-scale assessment of groundwater depletion and related groundwater abstractions: Combining hydrological modeling with information from well observations and GRACE satellites. *Water Resources Research*, *50*(7), 5698-5720. https://doi.org/10.1002/2014WR015595

Fan, Y., Li, H., & Miguez-Macho, G. (2013). Global Patterns of Groundwater Table Depth. *Science*, *339*(6122), 940-943. https://doi.org/10.1126/science.1229881

Gleeson, T., Moosdorf, N., Hartmann, J., & van Beek, L. P. H. (2014). A glimpse beneath earth's surface: GLobal HYdrogeology MaPS (GLHYMPS) of permeability and porosity. *Geophysical Research Letters*, *41*(11), 3891-3898. https://doi.org/10.1002/2014GL059856

Gleeson, T., Wada, Y., Bierkens, M. F. P., & van Beek, L. P. H. (2012). Water balance of global aquifers revealed by groundwater footprint. *Nature*, *488*(7410), 197-200. https://doi.org/10.1038/nature11295

Graham, N. T., Davies, E. G. R., Hejazi, M. I., Calvin, K., Kim, S. H., Helinski, L., Miralles-Wilhelm, F. R., Clarke, L., Kyle, P., Patel, P., Wise, M. A., & Vernon, C. R. (2018). Water Sector Assumptions for the Shared Socioeconomic Pathways in an Integrated Modeling Framework. *Water Resources Research*, *54*(9), 6423-6440. https://doi.org/10.1029/2018WR023452

Hanasaki, N., Yoshikawa, S., Pokhrel, Y., & Kanae, S. (2018). A global hydrological simulation to specify the sources of water used by humans. *Hydrol. Earth Syst. Sci.*, *22*(1), 789-817. https://doi.org/10.5194/hess-22-789-2018

Hanea, A., Morales Napoles, O., & Ababei, D. (2015). Non-parametric Bayesian networks: Improving theory and reviewing applications. *Reliability Engineering and System Safety*, *144*, 265-284. https://doi.org/https://doi.org/10.1016/j.ress.2015.07.027

Hejazi, M., Edmonds, J., Chaturvedi, V., Davies, E., & Eom, J. (2013). Scenarios of global municipal water-use demand projections over the 21st century. *Hydrological Sciences Journal*, *58*(3), 519-538. https://doi.org/10.1080/02626667.2013.772301

Hejazi, M., Edmonds, J., Clarke, L., Kyle, P., Davies, E., Chaturvedi, V., Wise, M., Patel, P., Eom, J., Calvin, K., Moss, R., & Kim, S. (2014). Long-term global water projections using six socioeconomic scenarios in an integrated assessment modeling framework. *Technological Forecasting and Social Change*, *81*, 205-226. https://doi.org/10.1016/j.techfore.2013.05.006

Jones, E., Qadir, M., van Vliet, M. T. H., Smakhtin, V., & Kang, S.-m. (2019). The state of desalination and brine production: A global outlook. *Science of The Total Environment*, *657*, 1343-1356. https://doi.org/10.1016/j.scitotenv.2018.12.076

Kim, S. H., Hejazi, M., Liu, L., Calvin, K., Clarke, L., Edmonds, J., Kyle, P., Patel, P., Wise, M., & Davies, E. (2016). Balancing global water availability and use at basin scale in an integrated assessment model. *Climatic Change*, *136*(2), 217-231. https://doi.org/10.1007/s10584-016-1604-6

Konikow, L. F. (2011). Contribution of global groundwater depletion since 1900 to sea-level rise. *Geophysical Research Letters*, *38*(17). https://doi.org/10.1029/2011GL048604

Kyle, P., Hejazi, M., Kim, S., Patel, P., Graham, N., & Liu, Y. (2021). Assessing the future of global energy-for-water. *Environmental Research Letters*, *16*(2), 024031. https://doi.org/10.1088/1748-9326/abd8a9

Lamontagne, J. R., Reed, P. M., Link, R., Calvin, K. V., Clarke, L. E., & Edmonds, J. A. (2018). Large Ensemble Analytic Framework for Consequence-Driven Discovery of Climate Change Scenarios. *Earth's Future*, *6*(3), 488-504. https://doi.org/10.1002/2017EF000701

Liu, Y., Hejazi, M., Kyle, P., Kim, S. H., Davies, E., Miralles, D. G., Teuling, A. J., He, Y., & Niyogi, D. (2016). Global and Regional Evaluation of Energy for Water. *Environmental Science & Technology*, *50*(17), 9736-9745. https://doi.org/10.1021/acs.est.6b01065

Liu, Y., Hejazi, M., Li, H., Zhang, X., & Leng, G. (2018). A hydrological emulator for global applications – HE v1.0.0. *Geosci. Model Dev.*, *11*(3), 1077-1092. https://doi.org/10.5194/gmd-11-1077-2018

Moss, R. H., Edmonds, J. A., Hibbard, K. A., Manning, M. R., Rose, S. K., van Vuuren, D. P., Carter, T. R., Emori, S., Kainuma, M., Kram, T., Meehl, G. A., Mitchell, J. F. B., Nakicenovic, N., Riahi, K., Smith, S. J., Stouffer, R. J., Thomson, A. M., Weyant, J. P., & Wilbanks, T. J. (2010). The next generation of scenarios for climate change research and assessment. *Nature*, *463*(7282), 747-756. https://doi.org/10.1038/nature08823

Niazi, M. H. K. (2019). *Flood Risk Prediction under Global Vegetated Hydrodynamics: A Bayesian Network* Delft University of Technology]. Netherlands. https://repository.tudelft.nl/islandora/object/uuid:ce7911c6-faa3-489f-8425-f08b2b9846fc

Niazi, M. H. K., Morales Nápoles, O., & van Wesenbeeck, B. K. (2021). Probabilistic Characterization of the Vegetated Hydrodynamic System Using Non-Parametric Bayesian Networks. *Water*, *13*(4). https://doi.org/10.3390/w13040398

O'Neill, B. C., Kriegler, E., Riahi, K., Ebi, K. L., Hallegatte, S., Carter, T. R., Mathur, R., & van Vuuren, D. P. (2014). A new scenario framework for climate change research: The concept of shared socioeconomic pathways. *Climatic Change*, *122*(3), 387-400. https://doi.org/10.1007/s10584-013-0905-2

Oki, T., & Kanae, S. (2006). Global Hydrological Cycles and World Water Resources. *Science*, *313*(5790), 1068-1072. https://doi.org/10.1126/science.1128845

Pokhrel, Y. N., Hanasaki, N., Yeh, P. J. F., Yamada, T. J., Kanae, S., & Oki, T. (2012). Model estimates of sea-level change due to anthropogenic impacts on terrestrial water storage. *Nature Geoscience*, *5*(6), 389-392. https://doi.org/10.1038/ngeo1476

Pokhrel, Y. N., Koirala, S., Yeh, P. J. F., Hanasaki, N., Longuevergne, L., Kanae, S., & Oki, T. (2015). Incorporation of groundwater pumping in a global Land Surface Model with the representation of human impacts. *Water Resources Research*, *51*(1), 78-96. https://doi.org/10.1002/2014WR015602

Riahi, K., van Vuuren, D. P., Kriegler, E., Edmonds, J., O'Neill, B. C., Fujimori, S., Bauer, N., Calvin, K., Dellink, R., Fricko, O., Lutz, W., Popp, A., Cuaresma, J. C., Kc, S., Leimbach, M., Jiang, L., Kram, T., Rao, S., Emmerling, J., . . . Tavoni, M. (2017). The Shared Socioeconomic Pathways and their energy, land use, and greenhouse gas emissions implications: An overview. *Global Environmental Change*, *42*, 153-168. https://doi.org/10.1016/j.gloenvcha.2016.05.009

Richts, A., Struckmeier, W. F., & Zaepke, M. (2011). WHYMAP and the Groundwater Resources Map of the World 1:25,000,000. In J. A. A. Jones (Ed.), *Sustaining Groundwater Resources: A Critical Element in the Global Water Crisis* (pp. 159-173). Springer Netherlands. https://doi.org/10.1007/978-90-481-3426-7_10

Scanlon, B. R., Zhang, Z., Save, H., Sun, A. Y., Muller Schmied, H., van Beek, L. P. H., Wiese, D. N., Wada, Y., Long, D., Reedy, R. C., Longuevergne, L., Doll, P., & Bierkens, M. F. P. (2018). Global models underestimate large decadal declining and rising water storage trends relative to GRACE satellite data. *Proceedings of the National Academy of Sciences*, *115*(6), E1080-E1089. https://doi.org/10.1073/pnas.1704665115

Thomson, A. M., Calvin, K. V., Smith, S. J., Kyle, G. P., Volke, A., Patel, P., Delgado-Arias, S., Bond-Lamberty, B., Wise, M. A., Clarke, L. E., & Edmonds, J. A. (2011). RCP4.5: a pathway for stabilization of radiative forcing by 2100. *Climatic Change*, *109*(1), 77. https://doi.org/10.1007/s10584-011-0151-4

Turner, S. W. D., Hejazi, M., Yonkofski, C., Kim, S. H., & Kyle, P. (2019). Influence of Groundwater Extraction Costs and Resource Depletion Limits on Simulated Global Nonrenewable Water Withdrawals Over the Twenty-First Century. *Earth's Future*, *7*(2), 123-135. https://doi.org/10.1029/2018EF001105

van Dijk, A. I. J. M., Renzullo, L. J., Wada, Y., & Tregoning, P. (2014). A global water cycle reanalysis (2003-2012) merging satellite gravimetry and altimetry observations with a hydrological multi-model ensemble. *Hydrol. Earth Syst. Sci.*, *18*(8), 2955-2973. https://doi.org/10.5194/hess-18-2955-2014

Vernon, C. R., Hejazi, M. I., Turner, S. W., Liu, Y., Braun, C. J., Li, X., & Link, R. P. (2019). A global hydrologic framework to accelerate scientific discovery. *Journal of Open Research Software*, *7*(1). https://doi.org/10.5334/jors.245

von Lampe, M., Willenbockel, D., Ahammad, H., Blanc, E., Cai, Y., Calvin, K., Fujimori, S., Hasegawa, T., Havlik, P., Heyhoe, E., Kyle, P., Lotze-Campen, H., Mason d'Croz, D., Nelson, G. C., Sands, R. D., Schmitz, C., Tabeau, A., Valin, H., van der Mensbrugghe, D., & van Meijl, H. (2014). Why do global long-term scenarios for agriculture differ? An overview of the AgMIP Global Economic Model Intercomparison. *Agricultural Economics*, *45*(1), 3-20. https://doi.org/10.1111/agec.12086

Wada, Y., & Bierkens, M. F. P. (2014). Sustainability of global water use: past reconstruction and future projections. *Environmental Research Letters*, *9*(10), 104003. https://doi.org/10.1088/1748-9326/9/10/104003

Wada, Y., van Beek, L. P. H., Sperna Weiland, F. C., Chao, B. F., Wu, Y.-H., & Bierkens, M. F. P. (2012). Past and future contribution of global groundwater depletion to sea-level rise. *Geophysical Research Letters*, *39*(9). https://doi.org/10.1029/2012GL051230

Wada, Y., van Beek, L. P. H., van Kempen, C. M., Reckman, J. W. T. M., Vasak, S., & Bierkens, M. F. P. (2010). Global depletion of groundwater resources. *Geophysical Research Letters*, *37*(20). https://doi.org/10.1029/2010GL044571

Yoshikawa, S., Cho, J., Yamada, H. G., Hanasaki, N., & Kanae, S. (2014). An assessment of global net irrigation water requirements from various water supply sources to sustain irrigation: rivers and reservoirs (1960-2050). *Hydrol. Earth Syst. Sci.*, *18*(10), 4289-4310. https://doi.org/10.5194/hess-18-4289-2014